



PONTIFICIA UNIVERSIDAD CATOLICA DE CHILE

ESCUELA DE INGENIERIA

**DYNAMIC ANALYSIS OF STRUCTURES
WITH XY-FPS AND FPS ISOLATORS AND THE
INFLUENCE OF SSI UNDER UPLIFT
CONDITIONS**

FEDERICO VILCA

Thesis submitted to the Office of Research and Graduate Studies in
partial fulfillment of the requirements for the Degree of Master of Science in
Engineering

Advisor:

JOSE ALMAZAN

Santiago de Chile, October 2021

© MMXXI, Federico Vilca



PONTIFICIA UNIVERSIDAD CATOLICA DE CHILE
ESCUELA DE INGENIERIA

DYNAMIC ANALYSIS OF STRUCTURES WITH XY-FPS AND FPS ISOLATORS AND THE INFLUENCE OF SSI UNDER UPLIFT CONDITIONS

FEDERICO VILCA

Members of the Committee:

JOSE ALMAZAN

ROSITA JÜNEMANN

CLAUDIA MARIN

JOSE PEREZ

Thesis submitted to the Office of Research and Graduate Studies in
partial fulfillment of the requirements for the Degree of Master of Science in
Engineering

Santiago de Chile, October 2021

To my Parents Juana and Federico
who support me in all my endeavors,
my siblings Fatima, Noemi and Jesus
who inspire me daily, and my
grandparents who will be dearly
remembered.

ACKNOWLEDGEMENTS

I thank my family for the constant love and support.

I thank Professor Jose Almazan for providing me guidance, mentorship, and inspiration during my time at the Pontificia Universidad Catolica de Chile. I remember the valuable time of learning when you explained me the behavior and implementation of the FPS and the XY-FPS step by step, with a great mood and patience.

I thank professors Claudia Marin, Rosita Jünemann, Jose Perez and Jose Almazan for serving on my committee and providing their valuable insight and feedback.

I thank Professor Juan Carlos de La Llera for providing me my first guidance at the Pontificia Universidad Catolica de Chile.

I thank my friends for illuminating my life with different kind of experiences.

I thank the Pontificia Universidad Catolica de Chile and the Department of Structural and Geotechnical Engineering for offering opportunities to both conduct research and gain invaluable teaching experience.

I thank the National Program of Scholarships and Educational Credits of Peru termed as PRONABEC through the International Scholarship Program for providing me an international scholarship and supported economically this research project, and the FONDECYT project N°1201841 for providing funding for this research project.

CONTENTS

ACKNOWLEDGEMENTS	iv
LIST OF TABLES	vii
LIST OF FIGURES.....	viii
ABSTRACT.....	xi
RESUMEN.....	xii
1. CONTEXT.....	1
2. COMPARISON OF THE LOCAL BEHAVIOUR OF THE XY-FPS AND THE FPS.....	7
2.1 Introduction.....	7
2.2 Equations used to evaluate the non-linear restoring force of the XY-FPS isolators.....	8
2.3 Interaction of pendular and frictional forces.....	14
3. COMPARISON OF THE DYNAMIC RESPONSE OF STRUCTURES WITH XY-FPS AND THE FPS	18
3.1 Models considered	18
3.2 Equations of motions and seismic ground motions considered	23
3.3 Results obtained	24
3.3.1 Results of model A	26
3.3.2 Results of model B.....	32
3.3.3 Results of model C.....	40
4. CONCLUSIONS	44

REFERENCES..... 46

LIST OF TABLES

	Pag.
3.1 Stiffness properties considered for the FPS and the XY-FPS in kN and m.	19
3.2 Parameters for determining spring stiffness and dashpot coefficients.....	22
3.3 Properties of the stiffness considered for the linear springs to represent the flexibility of the soil in kN and m.....	22
3.4 Properties of the damping coefficient considered for the linear dashpots to represent the flexibility of the foundation in kN and m.....	23
3.5 Earthquake records characteristic.....	24
3.6 Maximum uplift in cm ($\beta=0^\circ$).	33

LIST OF FIGURES

	Pag.
1.1 Application of the XY-FPS at the LA Emergency Operations Center.....	5
1.2 Typical Base Control System below apartment building.	5
1.3 Photo of installed CL bearing illustrating orthogonal LM guides assemblies on top and bottom.	6
2.1 A photograph of the tension-restraint friction pendulum isolator known as the XY-FPS device.	7
2.2 A schematic diagram of the tension-restraint friction pendulum isolator known as the XY-FPS device.....	8
2.3 (a) Isometric view of the XY-FPS in shape deformed, (b) and (c) Normal and frictional components in the local system acting on the sliding surface for plane 1-3 and 2-3, respectively, under compression.....	11
2.4 Pendulum effect for the XY-FPS and for the FPS bearing.....	15
2.5 Normalized frictional forces interaction diagram with constant vertical force F_3 and $D/R = 0.25$: (a) constant μ , and (b) $\mu_{max} = 2\mu_{min}$	16
2.6 Ratio q_μ between the maximum and minimum frictional resistance in the XY-FPS device.	17
3.1 Schematic representation of Model A: (a) with FPS; and (b) with XY-FPS....	18
3.2 Structural model of the 3D base-isolated structure (Model B and C). (a) Position of the isolators. (b) Elevation in x-direction. (c) Elevation in y-direction, units are in meters.....	20

3.3	Foundation model using in model C.....	21
3.4	Horizontal trajectory of the XY-FPS and the FPS for Model A ($T_s = 1.0$ s, $T_b = 2.5$ s) subjected to the Kobe earthquake record rotated at: a) $\beta = 0^\circ$; and b), $\beta = 45^\circ$	26
3.5	Horizontal trajectory of the XY-FPS and the FPS for Model A ($T_s = 1.0$ s, $T_b = 2.5$ s) subjected to the Newhall earthquake record rotated at: a) $\beta = 0^\circ$; and b) $\beta = 45^\circ$	26
3.6	Maximum horizontal displacements of the isolation systems. Colored bars represent the XY-FPS for $\beta = 0^\circ, 15^\circ, 30$ and 45° , black horizontal lines to the FPS devices.....	28
3.7	Maximum acceleration of the super-structure in X direction. Colored bars represent the XY-FPS, for $\beta = 0^\circ, 15^\circ, 30$ and 45° , black horizontal lines to the FPS devices.....	29
3.8	Response of PIR , PAR_y and PDR_y corresponding to Model A in Y direction. Colored bars represent the XY-FPS for $\beta = 0^\circ$ and 45° , and black horizontal lines represent the $PIR = 1$, the $PAR_y = 1$ and the $PDR_y = 1$, respectively, for $T_b = 2.5$ seconds	30
3.9	Response of PIR , PAR_y and PDR_y corresponding to Model A in Y direction. Colored bars represent the XY-FPS for $\beta = 0^\circ$ and 45° , and black horizontal lines represent the $PIR = 1$, the $PAR_y = 1$ and the $PDR_y = 1$, respectively, for $T_b = 5.0$ seconds.....	31
3.10	Horizontal trajectory of the isolator #4 for Model B ($T_b = 2.5$ s) subjected to the Kobe earthquake record rotated at: a) $\beta = 0^\circ$; and b) $\beta = 45^\circ$	32

3.11	Horizontal trajectory of the isolator #4 for Model B ($T_b = 5.0$ s) subjected to the Sylmar earthquake record rotated at: a) $\beta = 0^\circ$; and b) $\beta = 45^\circ$	32
3.12	Normalized normal forces corresponding to Model B ($\beta=0^\circ$).	34
3.13	Average floor PAR_y for $\beta = 0^\circ$ and 45°	36
3.14	Average floor PDR_y for $\beta = 0^\circ$ and 45°	37
3.15	Average floor peak acceleration [g] in XY-FPS System, in Y-direction, for $\beta = 0^\circ$ and 45°	38
3.16	Average floor peak effective drift [%] in XY-FPS System, in Y-direction, for $\beta = 0^\circ$ and 45°	39
3.17	Normalized axial force at different shear- wave velocity in the isolator # 1, for the model C with $T_b = 2.5$ s subjected to Lucerne record.....	41
3.18	Average floor peak acceleration ratio of each of floor considering the SSI in Y-direction - $P\hat{A}R(SSI)_y$ for $\beta = 0^\circ$	42
3.19	Average floor peak effective drift ratio of each of floor considering the SSI in Y-direction - $P\hat{D}R(SSI)_y$ for $\beta = 0^\circ$	43

ABSTRACT

Although today the positive effect of the use of seismic isolators in structures cannot be questioned, the efficacy of seismic isolation in structures subjected to strong ground excitation, including near-fault effects, is potentially compromised by situations that induce undesirable uplift in the isolation bearings. The XY-FPS is a type of friction pendulum isolator capable of resisting the forces of tension. This device consists of two sliding cylindrical surfaces, orthogonal to each other, and a mechanical unit that prevents uplift and connects the surfaces (rails), thus permitting movement in two directions independently.

This study attempts to answer the following questions: (i) what effects does the use of XY-FPS devices have on the three-dimensional seismic response of structures when compared to FPS devices, even when no uplift occurs; (ii) what is the magnitude of the tensile forces that are generated in slender structures with XY-FPS devices subjected to impulse-type earthquakes; (iii) what is the magnitude of the uplift and the impact forces in these same structures when using FPS devices; and (iv) what is the seismic response of structures considering the linear effect of soil flexibility using FPS devices.

Three structural models had been considered, referred to as A, B, and C. Model A corresponds to a single-storey building isolated with “one” isolator, when uplift does not occur. Model B is a 10-storey, plan symmetric reinforced concrete moment-frame structure, with eight isolators; and Model C is similar to Model B and considers only FPS isolators, including linear soil-structure interaction. A novel model of the XY-FPS isolator has been developed, incorporating full frictional coupling and large deformations. It is shown that the pendulum effect of the XY-FPS isolator is practically identical to the FPS, whereas the frictional effect in the XY-FPS isolator is strongly anisotropic. The results obtained with models A and B indicate that the maximum displacements of the XY-FPS isolators are not only smaller, but they are also very sensitive to the directionality of the seismic motion, when compared with their counterparts with FPS. In contrast, the superstructure response is higher for the structures with XY-FPS.

Keywords: XY-FPS; FPS; SSI; uplift; large deformations.

RESUMEN

Aunque actualmente el efecto positivo del uso de aisladores sísmicos en estructuras es no cuestionado, la eficacia del aislamiento sísmico en estructuras sometidas a una fuerte excitación del suelo, incluidos los efectos cercanos a la falla, se ve potencialmente afectada en situaciones que inducen levantamiento indeseable en los dispositivos de aislamiento sísmico. El XY-FPS es un tipo de aislador de péndulo friccional con capacidad de resistir fuerzas de tensión. Este dispositivo consta de dos superficies cilíndricas deslizantes, ortogonales entre sí, y una unidad mecánica que evita el levantamiento y conecta las superficies (rieles) permitiendo el movimiento en sus dos direcciones de forma independiente.

Este estudio intenta responder las siguientes preguntas: (i) qué efectos tiene el uso de los dispositivos XY-FPS en la respuesta sísmica tridimensional de las estructuras cuando se compara con los dispositivos FPS, incluso cuando no se produce ningún levantamiento; (ii) cuál es la magnitud de las fuerzas de tracción que se generan en estructuras esbeltas con dispositivos XY-FPS sometidos a terremotos de tipo impulsivo; y (iii) cuál es la magnitud del levantamiento y de las fuerzas de impacto en estas mismas estructuras cuando utilizan dispositivos FPS, y (iv) cuál es la respuesta sísmica de estructuras considerando el efecto lineal de la flexibilidad del suelo usando dispositivos FPS.

Se han considerado tres modelos estructurales, llamados A, B y C. El modelo A corresponde a un edificio de un solo piso con “un” aislador, cuando no se produce levantamiento. El modelo B, es una estructura simétrica de marco resistente a momento de hormigón armado de 10 pisos, con ocho aisladores; y el Modelo C es similar al Modelo B y considera solo aisladores FPS, incluida la interacción lineal suelo-estructura. Se ha desarrollado un modelo novedoso del aislador XY-FPS, que incorpora un acoplamiento friccional total y grandes deformaciones. Se muestra que el efecto pendular del aislador XY-FPS es prácticamente idéntico al del FPS, mientras que el efecto de friccional en el aislador XY-FPS es fuertemente anisotrópico. Los resultados obtenidos con los modelos A y B indican que los desplazamientos máximos de los aisladores XY-FPS no solo son menores, sino que también son muy sensibles a la direccionalidad del movimiento

sísmico, en comparación con su contraparte del FPS. Por el contrario, la respuesta de la superestructura es mayor para las estructuras con XY-FPS.

Palabras Claves: XY-FPS; FPS; SSI; levantamiento; deformaciones grandes.

1. CONTEXT

Although today the positive effect of the use of seismic isolators in structures cannot be questioned, the efficacy of seismic isolation in structures subjected to strong ground excitation, including near-fault effects, is potentially compromised by situations that induce undesirable uplift (or tension) in the isolation bearings. Development of tensile forces or uplift in isolation bearings may produce, under certain conditions, detrimental effects in the form of local instability or rupture of elastomeric bearings, and damage to sliding bearings due to large compressive forces on re-engagement following uplift. Loss of contact and impact on return can further yield higher-mode response and large axial forces in columns or in stiff walls (Roussis & Constantinou, 2006).

In point of fact, a variety of conditions may contribute to the development of either tensile forces or uplift. Typical examples include slender structures with large height-to-width aspect ratios, certain types of bridges with large ratios of height of the centroidal axis to the distance between the bearings, and buildings incorporating bearings below braced columns or stiff walls, and some local conditions such as soil structure interaction. Thus far, seismically-isolated structures have been designed so that uplift in sliding bearings or tension in elastomeric bearings is by-and-large avoided (Roussis & Constantinou, 2006).

The XY-FPS consists of two perpendicular steel beams (rails) and a mechanical unit that connects the rails, termed the connector. The connector resists tensile forces and slides to accommodate translation along the rails. Each rail has a sliding stainless steel concave surface: the lower-rail-concave surface faces up while the upper-rail-concave surface faces down. The connector provides resistance to tensile axial loads and intends to permit independent sliding in the two orthogonal directions (Marin, 2006). There are some structures and bridges that have been implemented with the XY-FPS around the world (Zayas, 2014). Figure 1.1 shows the LA Emergency Operations Center which was implemented with XY-FPS and FPS isolators in the City of Los Angeles.

Additionally, there are isolation systems which resist tensile force termed as the Base Control System (BCS) and the cross-linear (CL), the BCS consists of spring elements and

viscous dampers. These dampers supply absorption forces in all spatial directions (Nawrotzki, 2019). Figure 1.2 shows an example of a BCS below a reinforced concrete structure. The CL bearing allows nearly resistance-free linear motion (LM). The LM guide technology allows free rolling motion of a weight supporting part on a rail, where the part and the rail are internally separated by recirculating ball bearings. The CL bearing uses two orthogonally mounted LM guide assemblies as is depicted in Figure 1.3. The CL bearing can be combined with traditional isolation devices (Ryan, Coria & Dao, 2012). Recently, there is an alternative to achieve a more ductile response of the cross-laminated timber (CLT) using the post-tensioned rocking CLT panels coupled together with U-shaped flexural plate energy dissipation devices (UFPs), (Wichman, 2018). The concept for this system, typically referred to as the hybrid system, was originally developed for precast concrete structures (Stanton, Stone & Cheok, 1997; Restrepo, Mander & Holden, 2001; Hazaveh, Chase, Rodgers, Pampanin & Kordani, 2020; Bedriñana, Tani & Nishiyama, 2021); and some techniques of prestressing for the prevention of tensile force and uplift in bearings (Logiadis, 1996; Kasalanati & Constantinou, 1999), and there are some novel seismic isolation devices which reduce the effects of vertical impact (Auad & Almazan, 2021; Reyes & Almazan, 2020). Currently, there is a 3D seismic isolation system application in a narrow-built hospital to reduce the effects of vertical impacts and the effect of pounding (Nielsen, Rees, Dong, Chok, Fatemi & Zekioglu, 2017; Constantinou & Capen, 2019).

The first small-scale experimental studies of uplift behavior of narrow structures with different isolation systems concluded that the local behavior of these seismic isolation systems and the upper structure presented a good performance (Al-Huassaini, Zayas, & Constantinou, 1994 ; Griffith, Kelly, Coveney & Koh, 1988; Griffith, Aiken & Kelly, 1988). On the other hand, the influence of the vertical ground acceleration was found to have a minor effect on the response of the isolated bridges (Tsopelas & Constantinou, 1994; Mosqueda, Whittaker & Fenves, 2004).

A scaled experimental program has been studying the behaviour of a narrow structure seismically isolated with the XY-FPS and results from a number of tests conducted with combined horizontal and vertical excitations provided evidence of the effect of the vertical

component of ground motion on the response of the isolated structure (Roussis, 2004; Roussis & Constantinou, 2006). The results demonstrated that the vertical ground motion component had a minor effect on the isolation system displacement, although there was a non-negligible effect on the isolation system force response.

In addition, earthquake simulation tests of the XY-FPS isolated truss-bridge model was carried out (Marin, 2006). The results of the tests confirmed the early observations regarding the minor effect of vertical components of ground motion on the global structural response of the tension-resistant friction pendulum system. However, the peak shear forces of bearings can be significantly increased by the vertical component of the ground motion.

The experimental programs about seismic isolation systems mentioned before were scaled. However, there is a full-scale test of a 5-storey steel moment frame building that was carried out as part of a collaborative NEES/E-Defense research program. The building was tested in three configurations: isolated with triple friction pendulum bearings, isolated with lead rubber bearings combined with cross-linear sliders, and a fixed base (Dao, 2012; Ryan, Coria & Dao, 2012). It has been remarkable that the specimen isolated with triple friction pendulum bearings under 88% of the motion recorded at the Rinaldi receiving station during the Northridge earthquake, shows that every triple friction pendulum bearing uplifted at least once during the test series, and all but the southwest isolator uplifted. Further investigation indicated that the total vertical reaction subjected to this excitation was almost zero, synonymous with near total uplift of the whole building for a duration of about 0.1 seconds during this excitation. In the case of the specimen isolated with lead rubber bearings combined with cross linear sliders the test found that the largest compressive force in a single bearing was about 2000 kN (about 40% of the static weight of the building) and the largest tensile force was 453 kN, both observed during the motion recorded at Rinaldi. The variation in axial force during the Rinaldi ground motion was caused by the vertical excitation. In general, cavitation, or tensile rupture of the rubber matrix, is expected at a negative pressure = $3G$ (Constantinou et al, 2007), where G is the shear modulus of the rubber. Taking G to equal the design value of 0.41 MPa, the approximate tensile force for cavitation in these lead rubber bearings is 476 kN, which

only slightly exceeds the peak tensile force observed. Thus, the East lead rubber bearing may have been on the verge of cavitation, or cavitation may have actually occurred, preventing the peak tensile force from going beyond the observed value. However, the test program demonstrated the efficiency for both isolation systems in reducing the demands in the isolated structure. In addition, the specimen integrated suspended ceiling-partition wall-sprinkler piping system as part of the experimental program. In accordance with that, some level of damage was observed of these nonstructural elements with respect to the integrated system, which was directly related to the vertical component of input acceleration (Ryan, Soroushian, Maragakis, Sato, Sasaki & Okazaki, 2016). The test results show that the damage of the ceiling-partition-piping components initiated in the vertical acceleration of slabs between 2 and 3 g, moderate damage at vertical acceleration between 3 and 5 g, and extensive damage at vertical accelerations above 5 g.

The experimental full-scale program mentioned before which includes near fault grounds earthquake motions and the coupled of the vertical ground motions helping to understand the behaviour of the tension forces and uplift in seismic isolation devices different to the XY-FPS. Thus, ¿Is the XY-FPS the ideal isolator to improve the effects of tension forces and constrained uplift ?. According to the experimental scaled program, the effects of uplift of the FPS and the shear and tensile forces of the XY-FPS affect the local behaviour of each of ones and the response of the structure. That is why this study attempts to answer the following questions. First, what effects does the use of XY-FPS devices have on the three-dimensional seismic response of structures when compared to FPS devices, even when no uplift occurs. Second, what is the magnitude of the tensile forces that are generated in narrow structures with XY-FPS devices subjected to impulse-type earthquakes. Third, what is the magnitude of the uplift and the impact forces in these same structures when using FPS devices. And fourth what is the seismic response of structures considering the linear effect of soil flexibility using FPS devices.



Figure 1.1. Application of the XY-FPS at the LA Emergency Operations Center (<https://www.saifulbouquet.com/portfolio/los-angeles-emergency-operations-center/>)



Figure 1.2. Typical Base Control System below apartment building (Nawrotzki et al, 2019).



Figure 1.3. Photo of installed CL bearing illustrating orthogonal LM guides assemblies on top and bottom (Ryan et al, 2013).

2. COMPARISON OF THE LOCAL BEHAVIOUR OF THE XY-FPS AND THE FPS

2.1 Introduction

The XY-FPS typically has two orthogonal cylindrical rails interconnected by a housing-slider assembly. The housing slider assembly contains two cylindrical sliders, and the housing unit which structurally interconnects the two orthogonal rails and prevents uplift. Each rail has a sliding stainless steel concave surface: the lower-rail-concave surface faces up while the upper-rail-concave surface faces down. The XY-FPS is capable of carrying tension as well as compression loads and providing independent stiffness and energy dissipation along the principal horizontal directions of the bearing. The effective length and effective friction of the two pendulum mechanisms can be selected independently, to provide optimum performance. Figure 2.1 shows a photograph of the Tension-restraint friction pendulum isolator (XY-FPS) and Figure 2.2 depicts a schematic diagram of the tension-restraint friction pendulum isolator (XY-FPS). Further description of the mechanical characteristics of the behaviour of the tension restraint friction pendulum isolator is provided in Roussis and Constantinou.

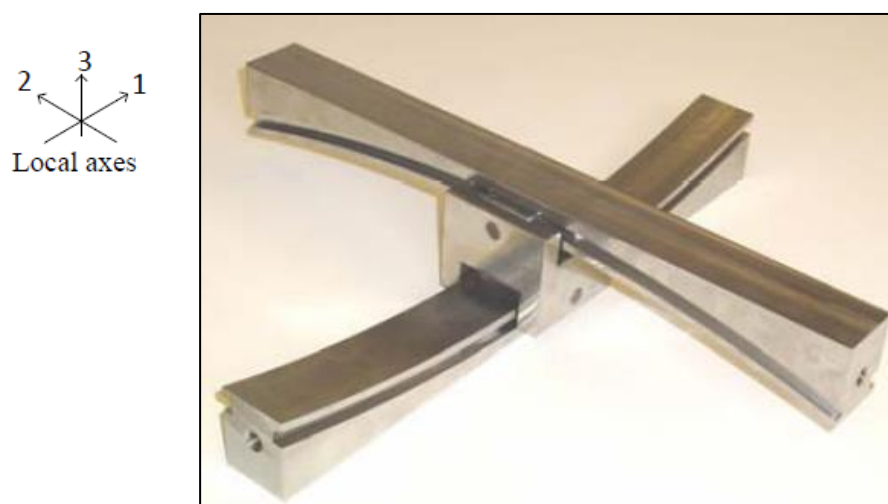


Figure 2.1. A photograph of the tension-restraint friction pendulum isolator known as the XY-FPS device (Huang et al, 2006).

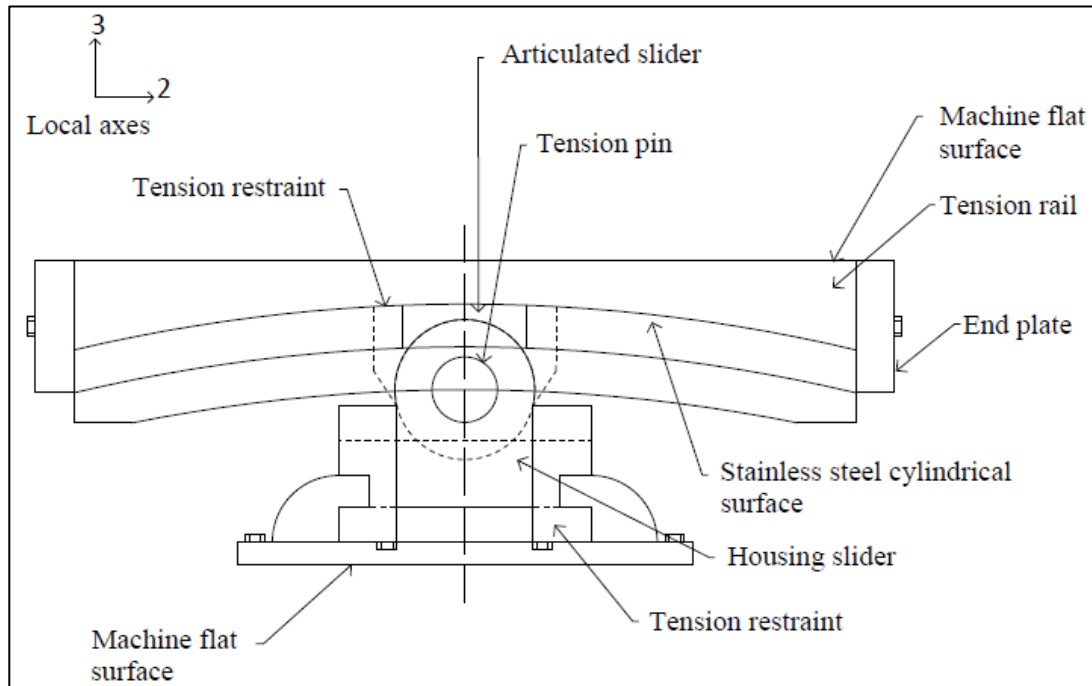


Figure 2.2. A schematic diagram of the tension-restraint friction pendulum isolator known as the XY-FPS device (Huang et al, 2006).

2.2 Equations used to evaluate the non-linear restoring force of the XY-FPS isolators

Structural analysis software is available such as SAP2000 (SAP2000. © 2021. Computers & Structures, Inc) and 3D-BASIS ME (Tsopelas, Constantinou & Reinhorn, 1994), which include an analytical model of the XY-FPS proposed by Roussis. However, this does not consider the bidirectional interaction between the shear force in one direction and the friction force in the other, and neither the formulation of the large deformations. In that context, it is important to propose a physical model of the XY-FPS that considers the characteristics mentioned before providing a better representation of the pendular and frictional effects of the XY-FPS.

The physical model of the XY-FPS isolator presented here follows the same logic of the physical model of the FPS developed in the reference: Physical model for dynamic analysis of structures with FPS isolators (Almazan & De la Llera, 2003).

Figure 2.3 shows a schematic view of the XY-FPS isolator in a deformed shape, the local axes 1 and 2 are oriented at the direction of bottom and top cylindrical sliding, respectively. However, local axe 3 is perpendicular to the previous ones.

To find the forces generated in the isolator, projected on its local axes, we analyzed the equilibrium in the deformed position by following the steps below:

Step 1: Compute the unit vectors associated with the normal and frictional forces generated at the cylindrical sliding surfaces.

$$\hat{\mathbf{n}}_1 = [\sin \theta_1 \quad 0 \quad -\cos \theta_1]^T \quad (2.1)$$

$$\hat{\mathbf{n}}_2 = [0 \quad -\sin \theta_2 \quad \cos \theta_2]^T \quad (2.2)$$

$$\hat{\mathbf{t}}_1 = -\text{sign}(\dot{D}_1) [\cos \theta_1 \quad 0 \quad \sin \theta_1]^T \quad (2.3)$$

$$\hat{\mathbf{t}}_2 = -\text{sign}(\dot{D}_2) [0 \quad -\cos \theta_2 \quad -\sin \theta_2]^T \quad (2.4)$$

where $\theta_1 = a \sin \frac{D_1}{R_1}$ and $\theta_2 = a \sin \frac{D_2}{R_2}$ are the angles between the bottom and the top sliding surfaces in normal directions and local axe 3.

Step 2: Compute the vertical deformation of the isolator

$$s = D_3 - (w_1 + w_2) \quad (2.5)$$

where $w_1 = R_1(1 - \cos \theta_1)$ and $w_2 = R_2(1 - \cos \theta_2)$ are the vertical relative displacements between sliders and the bottom and the top sliding surfaces, respectively.

Step 3: Compute the vertical force of the isolator

$$F_3 = \left(k_s^{(c)} U(-s) + k_s^{(t)} U(s) \right) s \quad (2.6)$$

Step 4: By applying the equilibrium of forces at local axe 3, compute the normal forces N_1 and N_2

$$N_1 = \frac{-F_3 + \mu_{12} \|F_2\| \sin \theta_1 \operatorname{sign}(\dot{D}_1)}{-\cos \theta_1 - \mu_1 \sin \theta_1 \operatorname{sign}(F_3)} \quad (2.7)$$

$$N_2 = \frac{F_3 - \mu_{21} \|F_1\| \sin \theta_2 \operatorname{sign}(\dot{D}_2)}{\cos \theta_2 + \mu_2 \sin \theta_2 \operatorname{sign}(F_3)} \quad (2.8)$$

Step 5: Finally; by applying the equilibrium at the directions of 2 and 3, compute the lateral forces F_1 and F_2 .

$$F_1 = -N_1 \sin \theta_1 + (\mu_1 \|N_1\| + \mu_{12} \|F_2\|) \cos \theta_1 \operatorname{sign}(\dot{D}_1) \quad (2.9)$$

$$F_2 = -N_2 \sin \theta_2 + (\mu_2 \|N_2\| + \mu_{21} \|F_1\|) \cos \theta_2 \operatorname{sign}(\dot{D}_2) \quad (2.10)$$

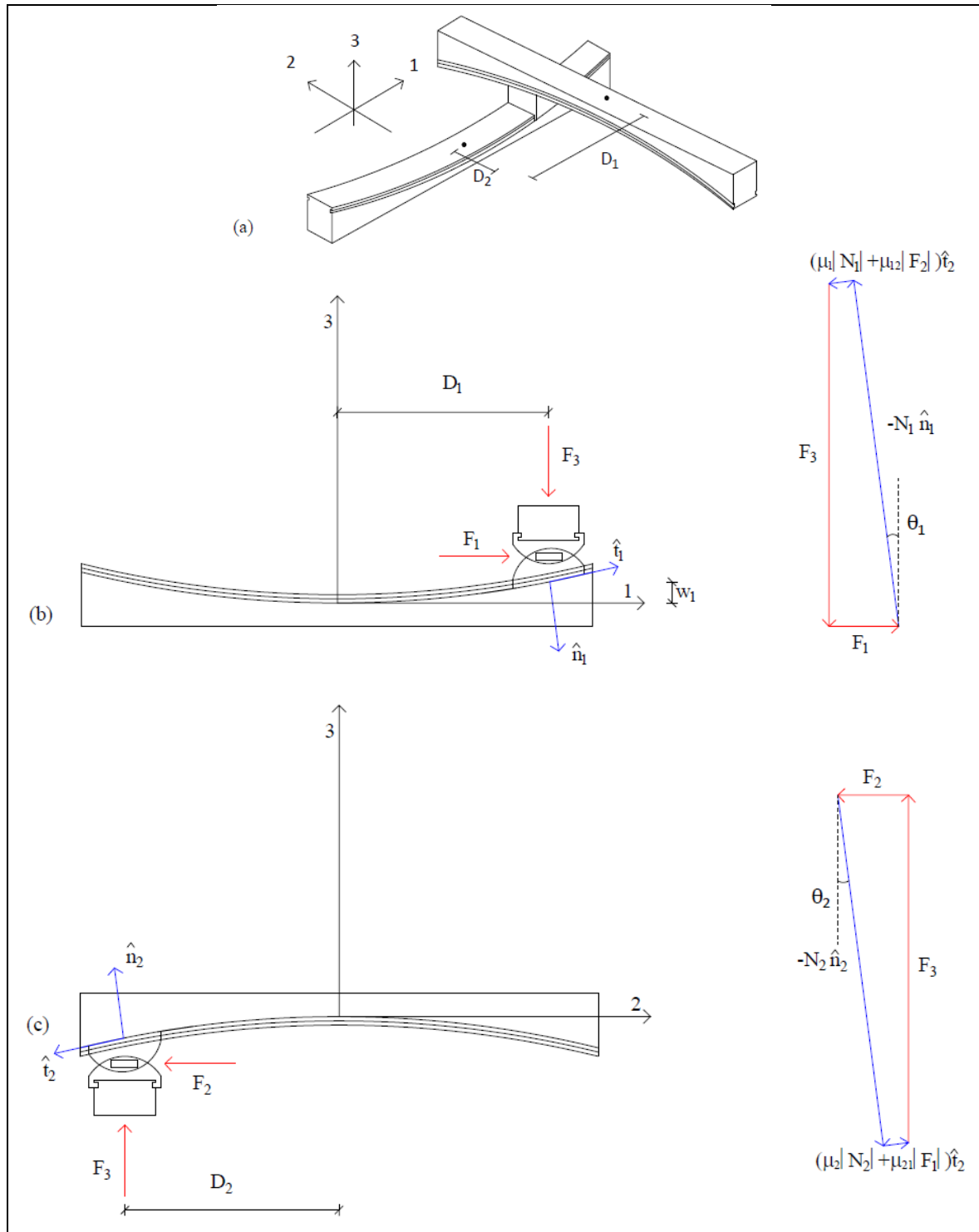


Figure 2.3. (a) Isometric view of the XY-FPS in shape deformed, (b) and (c) Normal and frictional components in the local system acting on the sliding surface for plane 1-3 and 2-3, respectively, under compression.

It can be noted from equations (2.7) to (2.10) that there are four nonlinear equations with four unknowns. However, these can be resolved using iterations considering a fixed point, while it is assumed at the beginning that $N_1=N_2=F_3$. Excellent precision can be obtained with just two iterations. Finally, considering $\sin \theta_1 = D_1/R_1$, $\sin \theta_2 = D_2/R_2$, $\cos \theta_1 = \sqrt{R_1^2 - D_1^2}/R_1$ and $\cos \theta_2 = \sqrt{R_2^2 - D_2^2}/R_2$, the final expressions are obtained:

$$F_1 = -\frac{N_1}{R_1}D_1 + (\mu_1\|N_1\| + \mu_{12}\|F_2\|)\frac{\sqrt{R_1^2 - D_1^2}}{R_1}\text{sign}(\dot{D}_1) \quad (2.11)$$

$$F_2 = -\frac{N_2}{R_2}D_2 + (\mu_2\|N_2\| + \mu_{21}\|F_1\|)\frac{\sqrt{R_2^2 - D_2^2}}{R_2}\text{sign}(\dot{D}_2) \quad (2.12)$$

$$F_3 = \left(k_s^{(c)}U(-s) + k_s^{(t)}U(s)\right)s \quad (2.13)$$

where F_1 and D_1 are the horizontal force and the horizontal displacement corresponding to the movement in the plane of symmetry 1-3 (bottom part, concave surface); N_1 is the corresponding normal force (positive in tension); R_1 and μ_1 are the radii of curvature and the coefficient of friction associated with the sliding cylindrical surface parallel to the 1-3 plane; F_2 and D_2 are the horizontal force and the horizontal displacement corresponding to the movement in the plane of symmetry 2-3 (upper part, convex surface); N_2 is the corresponding normal force (positive in tension); R_2 and μ_2 are the radii of curvature and the coefficient of friction associated with the sliding cylindrical surface parallel to the 2-3 plane; μ_{12} and μ_{21} are the coefficient of friction associated with the side contact surfaces between the connector and the rails of the bearing in the plane of 1-3 and 2-3, respectively; F_3 and s are the vertical force and the vertical deformation, $k_s^{(c)}$ and $k_s^{(t)}$ are the vertical stiffness in compression and tension, respectively, being $U(\cdot)$ the Heaviside function.

In the case of the FPS device, the following equations are considered (Almazan & De la Llera, 2003).

$$F_1 = \frac{N}{R}D_1 + \mu NZ_1 \quad (2.14)$$

$$F_2 = \frac{N}{R}D_2 + \mu NZ_2 \quad (2.15)$$

$$F_3 = k_s^{(c)}U(-s)s \quad (2.16)$$

where N is the normal force (positive in compression); R is the radii of curvature of the (spherical) FPS; D_1 and D_2 are the horizontal displacement corresponding to the local 1 and 2 directions, respectively; F_3 and s are the vertical force and the vertical deformation, with $k_s^{(c)}$ being the vertical stiffness (only compression); and μ is the coefficient of friction associated with the side contact surfaces and the slider of the bearing; Z_1 and Z_2 are the frictional hysteretic variables.

For reasons of simplicity, it has been assumed that the four friction coefficients corresponding to the XY-FPS isolator are equal to each other (both in compression and tension), and in turn equal to the value used for the FPS isolator. However, the variability of the friction coefficient with the sliding velocity v had been considered by means of the following equation (Constantinou, Mokha & Reinhorn, 1990) :

$$\mu = \mu_{max} - (\mu_{max} - \mu_{min}) \exp(-a\|v\|) \quad (2.17)$$

where μ_{max} and μ_{min} are the friction coefficients for large and low velocities, respectively, and a is a transition coefficient.

2.3 Interaction of pendulum and frictional forces

The first term in equations (2.11) and (2.12) represent the pendulum effect in the XY-FPS device. Similarly, the first term in equations (2.14) and (2.15) represent the pendulum effect in the FPS device. In both devices this (self-centering) effect is associated with the gravitational potential energy that they store due to vertical displacement. These displacements, w_{XY-FPS} and w_{FPS} , can be expressed as:

$$w_{XY-FPS} = R_1 \left(1 - \sqrt{1 - \frac{D_1^2}{R_1^2}} \right) + R_2 \left(1 - \sqrt{1 - \frac{D_2^2}{R_2^2}} \right) \quad (2.18)$$

$$w_{FPS} = R \left(1 - \sqrt{1 - \frac{D_1^2 + D_2^2}{R^2}} \right) \quad (2.19)$$

The values of w_{XY-FPS} and w_{FPS} as a function of D_1 and D_2 , assuming $R_1 = R_2 = R$, are presented in Figure 2.4. As can be seen, although the values of w_{XY-FPS} do not describe an exact spherical surface, the differences with w_{FPS} are negligible. Therefore, the XY-FPS device can be considered equivalent to the FPS in terms of the pendulum effect.

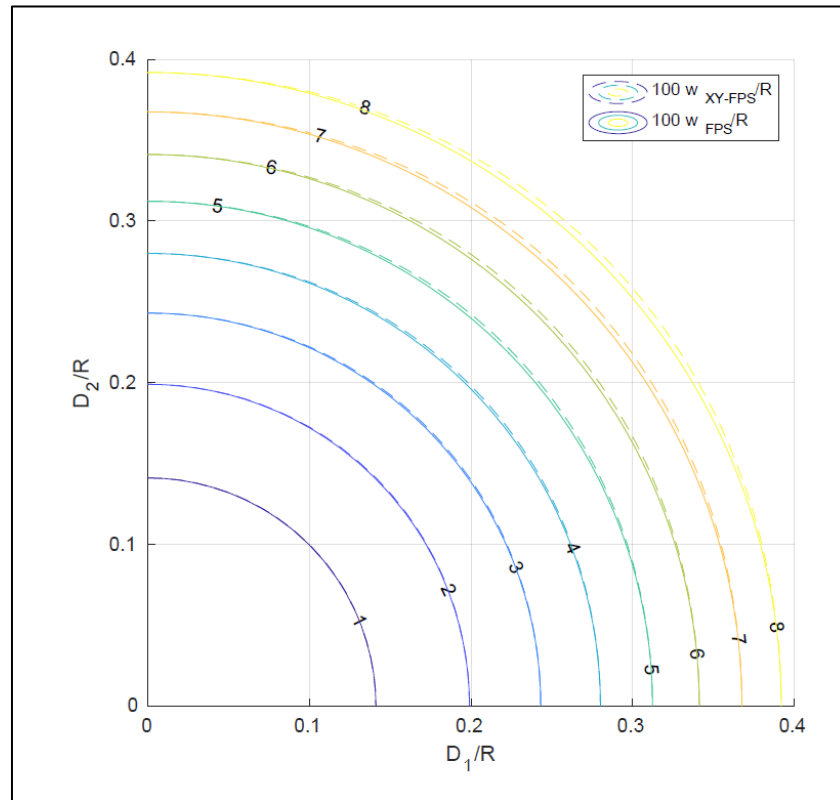


Figure 2.4. Pendulum effect for the XY-FPS and for the FPS bearing.

Furthermore, the second term in equations (2.11) and (2.12) represent the frictional effect in the XY-FPS device. Similarly, the second term in equations (2.14) and (2.15) represent the frictional effect in the FPS device. In order to compare the frictional behavior between both devices, equations 2.11 to 2.16 are solved assuming constant vertical force F_3 , and imposing unidirectional displacements in all directions, i.e. $D_1 = D \cos \alpha$ and $D_2 = D \sin \alpha$ ($0 \leq \alpha \leq 2\pi$). The frictional interaction diagram obtained with this analysis is shown in Figure 2.5, for constant ($\mu_{max} = \mu_{min}$) and variable ($\mu_{max} = 2\mu_{min}$) friction coefficient, and $D/R = 0.25$. It can be noted that the FPS has the same frictional resistance in every direction (isotropic). However, the XY-FPS has two axes of minimum frictional resistance in local direction 1 and 2 ($\alpha = 0, \pi/2$), and two axes of maximum frictional resistance ($\alpha = \pm\pi/4$). These four directions are the symmetry axes of the device.

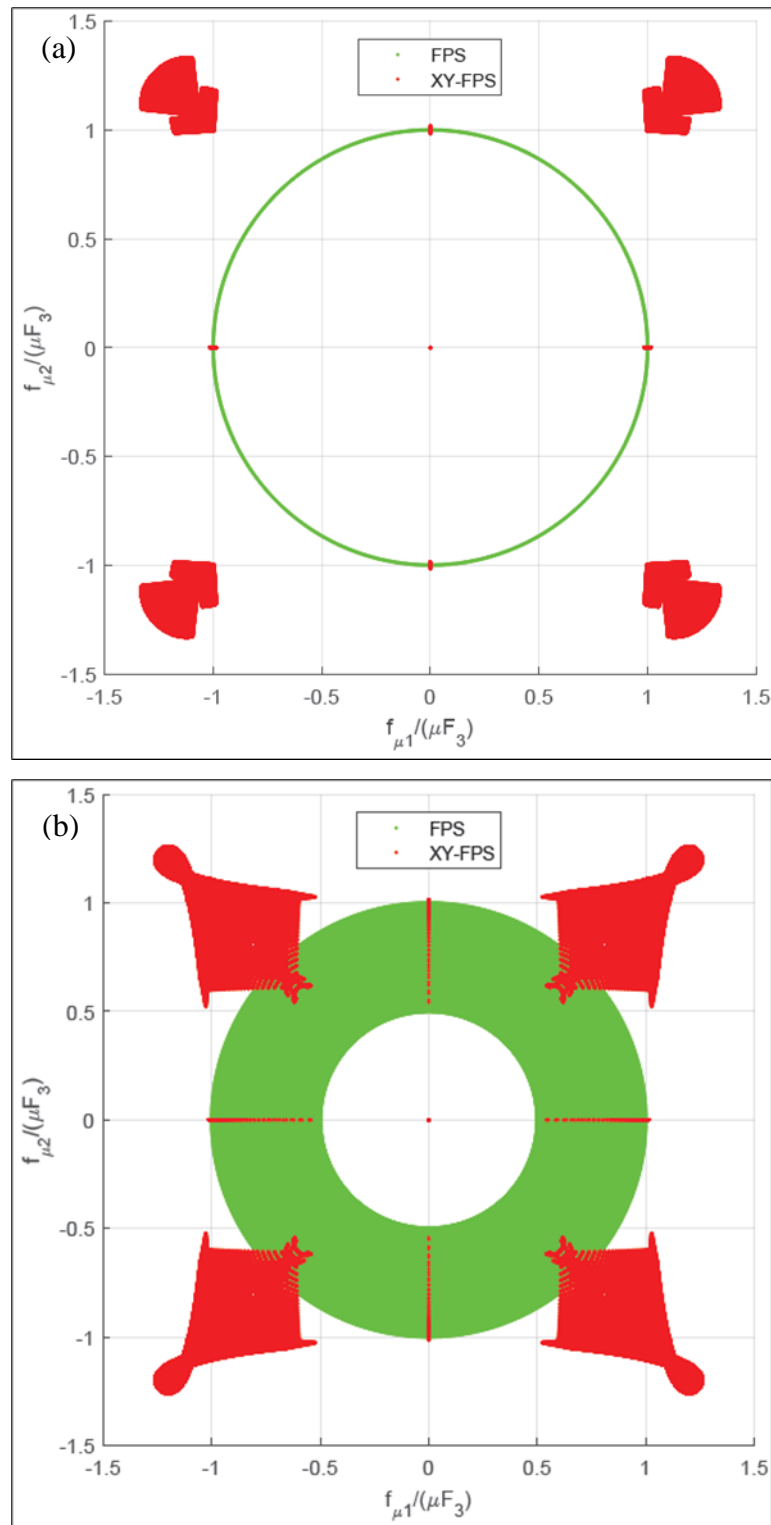


Figure 2.5. Normalized frictional forces interaction diagram with constant vertical force F_3 and $D/R = 0.25$: (a) constant μ , and (b) $\mu_{max} = 2\mu_{min}$.

In an approximate way, the ratio q_μ between the maximum and minimum frictional resistance f_μ in the XY-FPS device can be expressed as (Figure 2.6):

$$q_\mu = \frac{f_\mu(\alpha = \pi/4)}{f_\mu(\alpha = 0)} \approx \sqrt{2} \left(1 + \frac{\mu}{1 - \mu} \right) + \left(\frac{1}{1 - \mu} \right) \frac{D}{R} \quad (2.20)$$

It is evident that at higher levels of lateral displacement this ratio increases.

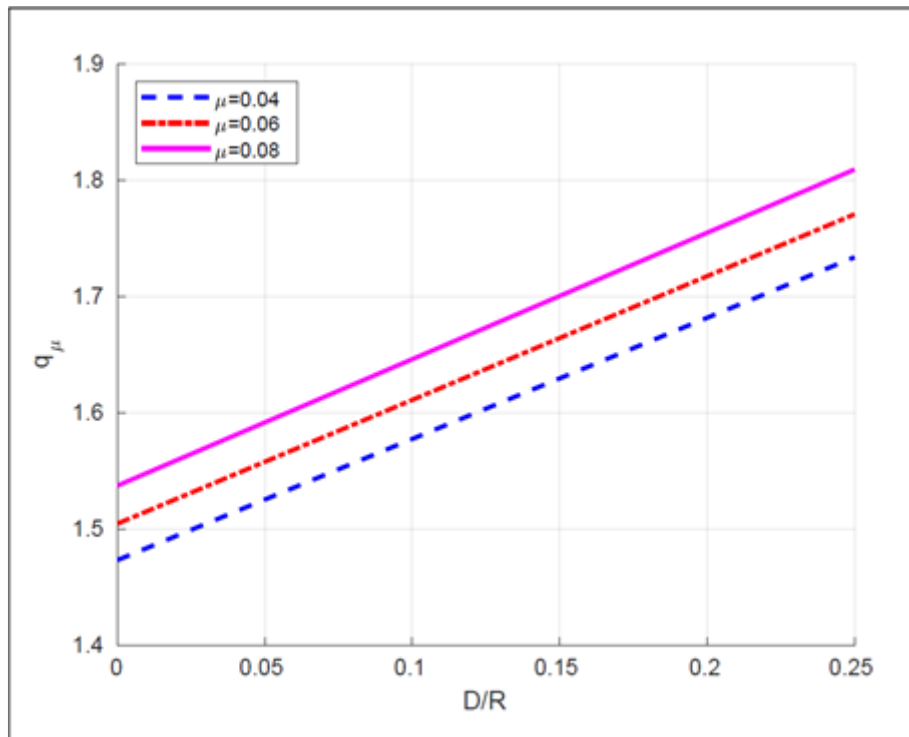


Figure 2.6. Ratio q_μ between the maximum and minimum frictional resistance in the XY-FPS device.

3. COMPARISON OF THE DYNAMIC RESPONSE OF STRUCTURES WITH XY-FPS AND THE FPS

3.1 Models considered

In this study three structural models were considered, referred to as Model A, B, and C. The structural models were fully developed in the MATLAB environment (MATLAB. © 1994-2021. The MathWorks, Inc.).

Model A corresponds to a single-storey building isolated with one isolator (FPS and XY-FPS), as shown in Figure 3.1. The masses of the structure and the base are m_s and m_b , respectively. The structural elements between the floor and isolation levels are modelled by linear springs and dashpot elements, in three perpendicular directions, the two horizontals of X , Y and the vertical Z . The physical parameters were calibrated to obtain fixed-base lateral periods $T_{sx} = T_{sy} = 0.2$ s, 0.4 s, 0.6 s, 0.8 s, and 1.0 s; a fixed-base vertical period $T_{sz} = 0.05$ s; and fixed-base damping ratio $\xi_s = 0.02$ in all directions. The isolation system was modeled to obtain nominal isolation periods $T_b = 2.5$ s and 5.0 s (i.e. $R = 1.55$ m and $R = 6.25$ m). The frictional behavior was modeled according to equation (2.7) assuming $\mu_{max} = 0.08$, $\mu_{min} = 0.04$, and $a = 20$ s/m.

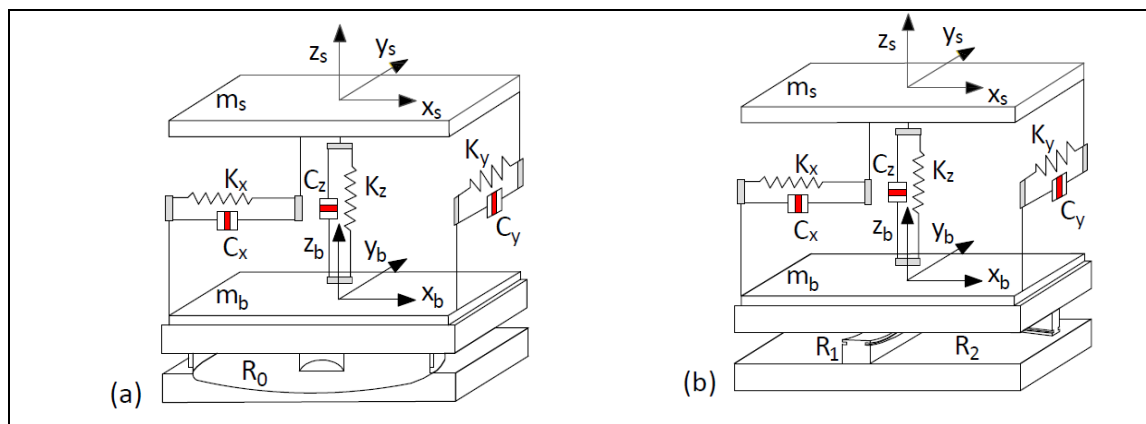


Figure 3.1. Schematic representation of Model A: (a) with FPS; and (b) with XY-FPS.

Table 3.1. shows the properties of stiffness considered for the FPS and the XY-FPS and Figure 3.2 represents the structural model of the 3D base-isolated structure for both model B and model C.

Model B is a 10-storey, 3-bay-by-1-bay, plan symmetric reinforced concrete moment-frame structure, with eight isolators. The bay width in both directions and the storey height were taken as 5.0 m and 3.0 m, respectively. The beams have rectangular sections of 40 cm x 60 cm, and the columns have square sections of 60 cm x 60 cm, and the slabs have a thickness of 15 cm.

The elastic modulus of the concrete was assumed as $E_c = 23.4 \text{ Gpa}$, the Poisson's ratio used was $\nu = 0.2$. A seismic weight of $w = 13.2 \text{ kN/m}^2$ was assigned to all storeys, leading to a total weight of $W_s = 10,890 \text{ kN}$. The superstructure was modeled as a 3D linear elastic multi-degree-of-freedom system. The coupling between the lateral and vertical motions of the frictional devices is able to activate modes of vibrations in the global $-Z$ direction. Due to this phenomenon, an appropriate mesh is necessary to accurately represent vertical dynamics, especially in the modelling of beams and slabs (Aquad & Almazan, 2021). The slabs were modeled using 297 shell elements with an area of 1.7 m x 1.7m. The beams were modeled using 330 frame elements with a length of 1.7 m. The columns were incorporated using 160 frame elements with a length of 1.5 m. A constant damping ratio of $\xi_s = 0.02$ was used in all non-isolated modes, and $\xi_i = 0.0$ in the first three isolated modes (Giammona, Ryan & Dao, 2015). The isolators were modeled with $R = 1.55 \text{ m}$ ($T_b = 2.5 \text{ s}$) and $R = 6.25 \text{ m}$ ($T_b = 5.0 \text{ s}$), $\mu_{max} = 0.070$, $\mu_{min} = 0.045$, and $a = 20 \text{ s/m}$.

Table 3.1. Stiffness properties considered for the FPS and the XY-FPS in kN and m.

Properties	FPS	XY-FPS
$k_3^{(c)}$	4930300	4930300
$k_3^{(t)}$	-	2465150
k_1	875.97	875.97
k_2	875.97	875.97
k_1^{NL}	190575	-

where k_1 and k_2 are the horizontal effective lateral stiffness in the local -1 and -2 directions respectively; and k_1^{NL} is the nonlinear stiffness.

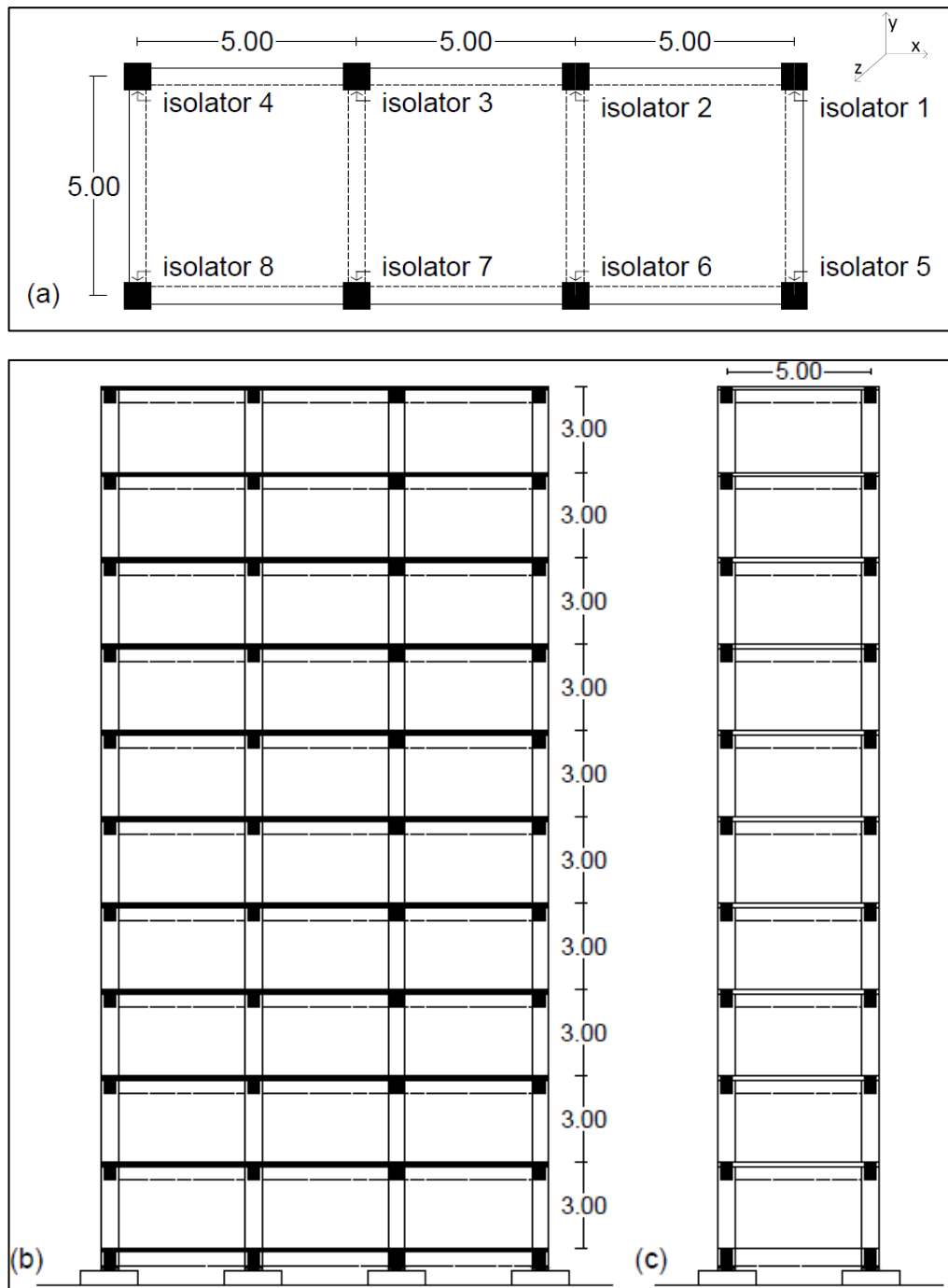


Figure 3.2. Structural model of the 3D base-isolated structure (Model B and C). (a) Position of the isolators. (b) Elevation in x-direction. (c) Elevation in y-direction, units are in meters.

Finally, Model C is similar to Model B and consider only FPS isolators, including linear soil-structure interaction.

For the SSI analysis, we will summarize the procedure made by Dao and Ryan, 2020 (for further details please consult Dao and Ryan, 2020). This study used the same procedure.

For simplicity, the single footings were treated as individual square foundations and were assumed to be rigid. These assumptions were used in previous investigations in conventional buildings (ATC and CUREE, 2012) and isolated buildings (Novak and Henderson, 1989). Based on these, springs, dashpots, masses, and moments of inertia representing the sub-structure system can be lumped to the bottom of the bearing element as shown in Figure 3.3. For simplicity, only degrees-of-freedom (DOFs) in the local axes 1 and 3 plane are shown in this figure. The mass of the footing m_f and the moment of inertia of the footing I_f are computed from the footing size and mass density. The stiffness K_i and damping coefficient C_i (where i takes the value 1, 2, 3 for translational DOFs in the respective local axes, or 11, 22, 33 for rotational DOFs about the respective local axes) were determined following (Pais & Kausel 1988). Input parameters for determining the stiffness and damping coefficient include mass density of soil ρ_s , effective shear wave velocity of soil V_s , Poisson's ratio of soil ν_s , half-width of footing B_f , half-length of footing L_f , depth of footing D_f , and dominant vibration period of the superstructure \tilde{T} with flexible foundation, which is dependent on K_i and can be obtained through an iteration process.

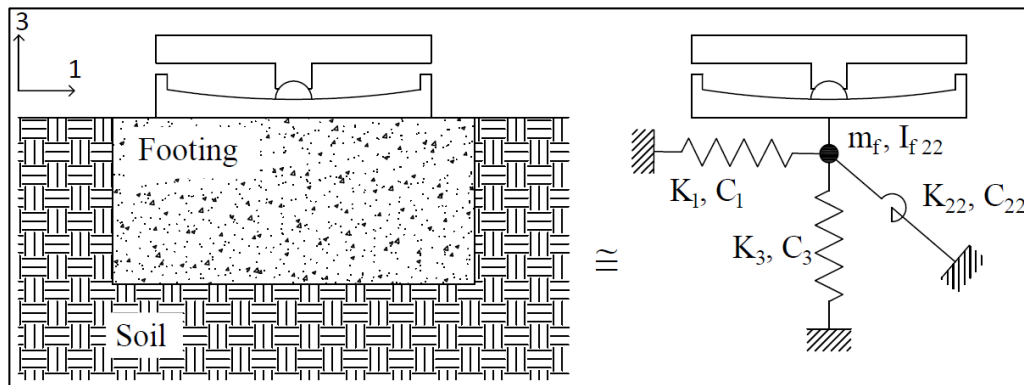


Figure 3.3. Foundation model using in model C.

The parameters of the soil are shown in Table 3.2 and the values of linear springs and damping coefficients are presented in Table 3.3 and 3.4, respectively. K_i is the frequency-dependent stiffness of the footing-soil spring in the six i -DOFs, which account for the embedment of the footing in the soil medium, and C_i represents the damping coefficients which includes the viscous damping (which represents radiation damping of soil) and hysteretic damping of soil.

Table 3.2. Parameters for determining spring stiffness and dashpot coefficients.

Parameter	Unit	Value
Mass density of soil, ρ_s	kg/m^3	2000
Shear wave velocity of soil, V_s	m/s	200 to 1000
Poisson's ratio of soil, ν_s	-	0.33
Hysteresis damping ratio of soil, β_s	-	0.05
Size of footing, $B_f \times L_f$	$m \times m$	2.5×2.5
Depth of footing, D_f	m	1.0

Table 3.3. Properties of the stiffness considered for the linear springs to represent the flexibility of the soil in kN and m.

$V_s(m/s)$	K_1	K_2	K_3	K_{11}	K_{22}	K_{33}
200	910600	910600	891100	2147900	2147900	3673000
300	2048800	2048800	2009500	4832900	4832900	8264500
400	3642000	3642000	3576000	8592000	8592000	14693000
1000	22764000	22764000	22379000	53700000	53700000	91831000

Table 3.4. Properties of the damping coefficient considered for the linear dashpots to represent the flexibility of the foundation in kN and m.

	$V_s(m/s)$	C_1	C_2	C_3	C_{11}	C_{22}	C_{33}
Kobe	200	47300	47300	8300	102080	102080	174530
	300	103330	103330	13540	229330	229330	392140
	400	180940	180940	19600	407510	407510	696840
	1000	1099900	1099900	73400	2545900	2545900	4353700
Newhall	200	56890	56890	8300	124700	124700	213210
	300	124900	124900	13540	280220	280220	479160
	400	219280	219280	19600	497960	497960	851530
	1000	1339500	1339500	73400	3111300	3111300	5320500
Sylmar	200	47300	47300	8300	102080	102080	174530
	300	103330	103330	13540	229330	229330	392140
	400	180940	180940	19600	407510	407510	696840
	1000	1099900	1099900	73400	2545900	2545900	4353700
Lucerne	200	63500	63500	8300	140300	140300	239880
	300	139780	139780	13540	315320	315320	539180
	400	245740	245740	19600	560360	560360	958230
	1000	1504900	1504900	73400	3501300	3501300	5987400

3.2 Equations considered for motions and seismic ground motions

The discrete non-linear equation of the motion of the structure subjected to seismic motion, can be written as follows:

$$\mathbf{M}\ddot{\mathbf{q}}(t) + \mathbf{C}\dot{\mathbf{q}}(t) + \mathbf{K}\mathbf{q}(t) + \mathbf{L}_f^T \mathbf{F}_u(t) = -\mathbf{M}\mathbf{S}\ddot{\mathbf{r}}_g(t) \quad (3.1)$$

where $\mathbf{q}_{\{nx1\}} = [q_1, \dots, q_i, \dots, q_n]^T$ is the vector of degrees of freedom (DOFs) of the structure; \mathbf{M} , \mathbf{C} and \mathbf{K} are the $n \times n$ well known mass, damping and stiffness matrices, respectively; \mathbf{F}_u is the vector of nonlinear forces of the isolators; \mathbf{L}_f is a kinematic transformation matrix, $\mathbf{L}_f^T \mathbf{F}_u$ is the vector of the non-linear restoring forces generated by the isolators with respect to the DOFs \mathbf{q} of the structure; $\ddot{\mathbf{r}}_g = [\ddot{u}_{gx} \ \ddot{u}_{gy} \ \ddot{u}_{gz} + g]^T$ is the vector of ground acceleration, where \ddot{u}_{gi} is the i th component of ground acceleration, and g represents the gravity and \mathbf{S} is the incidence matrix.

The ground motion records considered are shown in Table 3.5. It should be noted that the horizontal components of these records have been rotated to consider the effect of directionality in the response. This effect is particularly important in structures with XYFPS, due to the anisotropy in frictional resistance (see figures 2.5 and 2.6). Previous studies in XY-FPS considered impulsive earthquake ground motions (Roussis, 2004; Roussis & Constantinou, 2006; Marin, 2006) like this study.

Table 3.5. Earthquake records characteristics.

Ground Motion ID	Earthquake name	Year	Magnitude (Mw)	Component	PGA (g)
GM1	Newhall	1995	6.7	X-dir.	0.59
				Y-dir.	0.58
				Z-dir.	0.55
GM2	Sylmar	1995	6.7	X-dir.	0.84
				Y-dir.	0.60
				Z-dir.	0.54
GM3	Lucerne	1992	7.5	X-dir.	0.73
				Y-dir.	0.81
				Z-dir.	0.86
GM4	Kobe	1995	7.2	X-dir.	0.83
				Y-dir.	0.63
				Z-dir.	0.34

3.3 Results obtained

In this chapter, the main results obtained for the three models considered are presented, emphasizing the comparison between the responses obtained with the two devices, both for the isolation system and the superstructure. In order to establish an objective comparison, the following relationships between the maximum time-history responses are defined:

$$PIR = \frac{D_o^{(XY-FPS)}}{D_o^{(FPS)}} \quad (3.2)$$

$$PAR_x = \frac{a_{xo}^{(XY-FPS)}}{a_{xo}^{(FPS)}} \quad (3.3)$$

$$PAR_y = \frac{a_{yo}^{(XY-FPS)}}{a_{yo}^{(FPS)}} \quad (3.4)$$

$$PDR_x = \frac{d_{xo}^{(XY-FPS)}}{d_{xo}^{(FPS)}} \quad (3.5)$$

$$PDR_y = \frac{d_{yo}^{(XY-FPS)}}{d_{yo}^{(FPS)}} \quad (3.6)$$

where PIR is the peak isolation ratio, being $D_o^{(XY-FPS)}$ and $D_o^{(FPS)}$ the peak absolute horizontal displacement of the XY-FPS and FPS devices, respectively; PAR_j is the $-j$ direction peak acceleration ratio ($j = X, Y$), being $a_{jo}^{(XY-FPS)}$ and $a_{jo}^{(FPS)}$ the $-j$ direction peak absolute acceleration of the superstructure with XY-FPS and FPS isolation devices, respectively; and PDR_j is the $-j$ direction peak drift ratio, being $d_{jo}^{(XY-FPS)}$ and $d_{jo}^{(FPS)}$ the $-j$ direction peak inter-storey drift of the superstructure with XY-FPS and FPS isolation devices, respectively.

Another important aspect to consider in the comparisons is the effect of the directionality of the ground motion. Incidence angles $\beta = 0^\circ, 15^\circ, 30^\circ$ and 45° have been considered, where β is the angle between the main direction of the seismic record (the one that produces the greatest displacement in the isolation system) with the global $-X$ axis of the structure.

3.3.1 Results of model A

The horizontal trajectory of the isolation system of a structure with $T_s = 1.0$ s and $T_b = 2.5$ s, subjected to the Kobe earthquake record, and rotated at $\beta = 0^\circ$ and $\beta = 45^\circ$ is presented in Figure 3.4. In both cases, it can be observed that the displacements of the structure with XY-FPS are smaller, which is a consequence of the greater frictional resistance of this device.

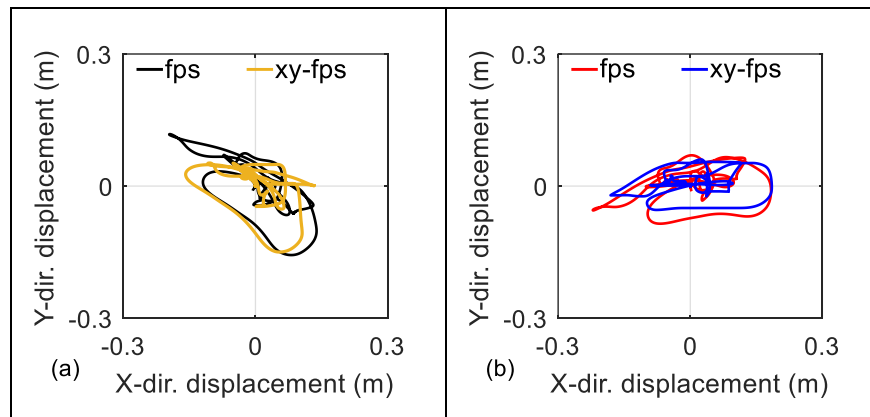


Figure 3.4. Horizontal trajectory of the XY-FPS and the FPS for Model A ($T_s = 1.0$ s, $T_b = 2.5$ s) subjected to the Kobe earthquake record rotated at: a) $\beta = 0^\circ$; and b), $\beta = 45^\circ$.

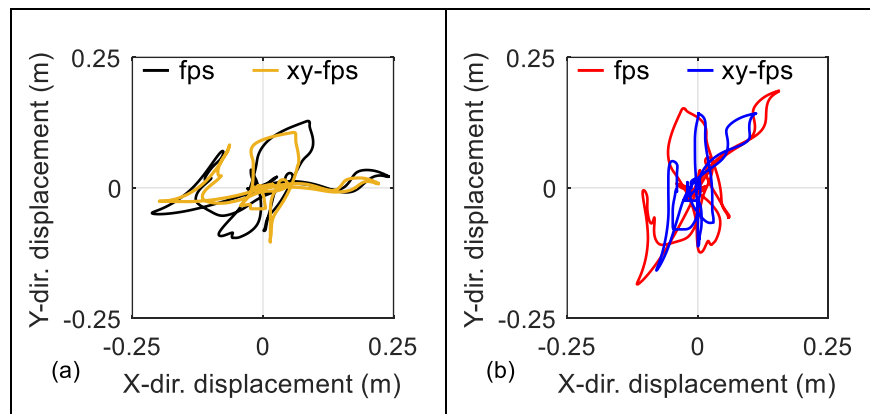


Figure 3.5. Horizontal trajectory of the XY-FPS and the FPS for Model A ($T_s = 1.0$ s, $T_b = 2.5$ s) subjected to the Newhall earthquake record rotated at: a) $\beta = 0^\circ$; and b) $\beta = 45^\circ$.

However, this effect is more noticeable for $\beta = 0^\circ$, as the trajectory of the structure with FPS tends to be oriented with an angle of 45° , which corresponds to the direction of maximum frictional resistance of the XY-FPS device. A similar result is presented in Figure 3.5, for the same structure, subjected to the Newhall record. In this case, the effect of reducing displacement is more noticeable for $\beta = 45^\circ$.

The maximum horizontal displacements of the isolation system corresponding to model A, subjected to the 4 seismic records considered, and with different angles of incidence, is shown in Figure 3.6. As expected, these results confirm what has been shown previously in figures 3.4 and 3.5. In other words, the maximum displacements of the XY-FPS isolators are not only smaller, but they are also very sensitive to the directionality of the seismic motion.

The maximum horizontal acceleration of the super-structure corresponding to Model A, subjected to the 4 seismic records, and with different angles of incidence, is shown in Figure 3.7. In contrast to what was observed in the isolation system, the superstructure accelerations are higher for the structures with XY-FPS. This should not be surprising, since in general the lower the friction in the isolation system, the greater the response of the superstructure. However, there is an additional effect, which is the greater tendency of the XY-FPS to stick on one of the two cylindrical sliding surfaces, producing trajectories with sudden changes in direction (spiky-shaped trajectory). This happens because of the device tends to slide at the minimum frictional resistance directions, which are the parallel directions to the cylindrical surfaces (as shown in Figure 2.5). Instead, the FPS system tends to move in more rounded trajectories, as is shown in Figures 3.4 and 3.5, due to the FPS has the same frictional resistance in every direction (isotropic).

Finally, Figure 3.8 and Figure 3.9 show the relationships between maximum responses defined in equations 3.2 to 3.6, for the four seismic records considered. As a general rule it can be observed that the lower the PIR values (below values when the $PIR = 1$), the higher the PAR_y and PDR_y values (over values when the $PAR_y = 1$ and the $PDR_y = 1$). Model A does not present uplift.

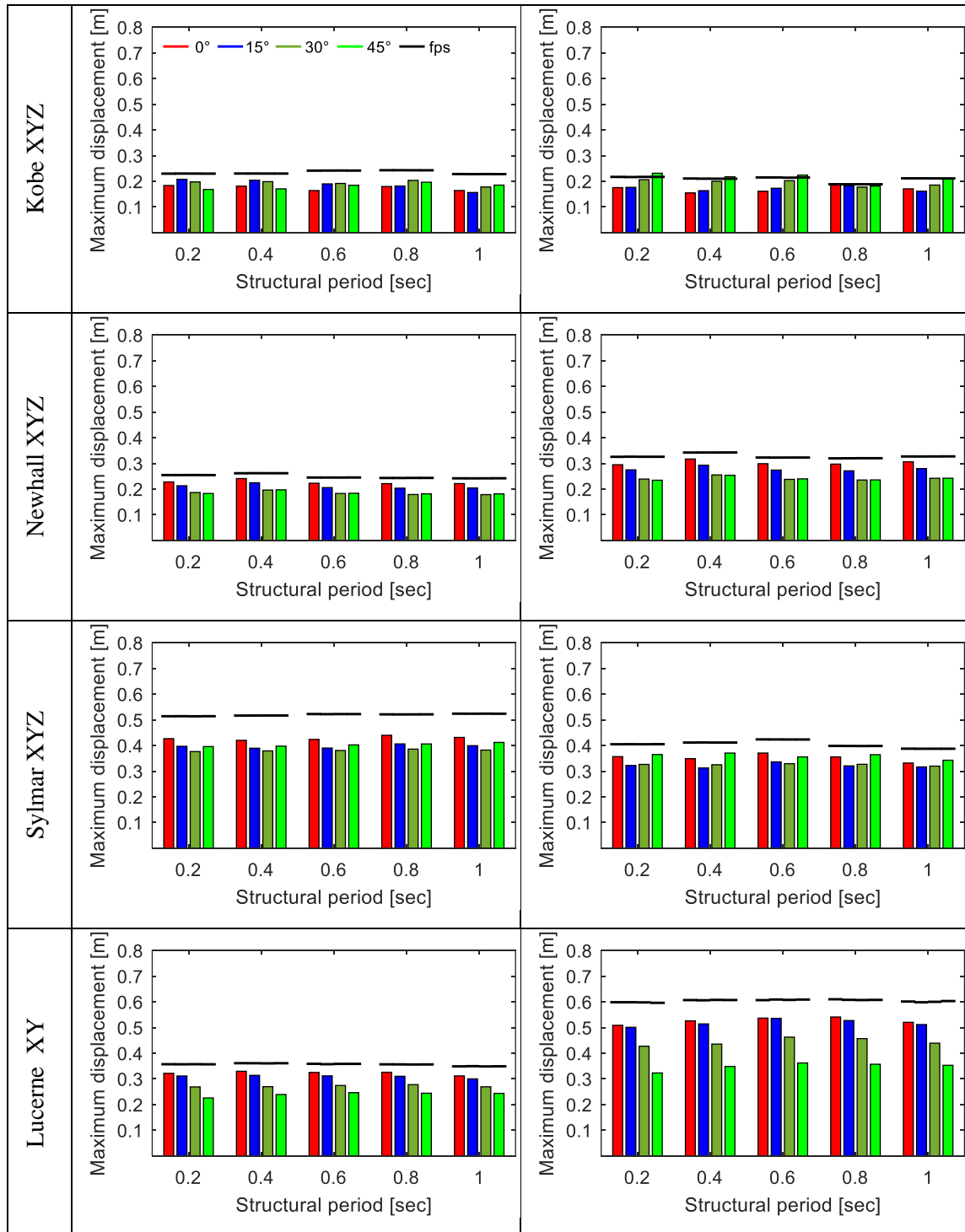


Figure 3.6. Maximum horizontal displacements of the isolation systems. Colored bars represent the XY-FPS for $\beta = 0^\circ, 15^\circ, 30^\circ$ and 45° , black horizontal lines to the FPS devices, $T_b = 2.5$ s (on the left) and $T_b = 5.0$ s (on the right) .

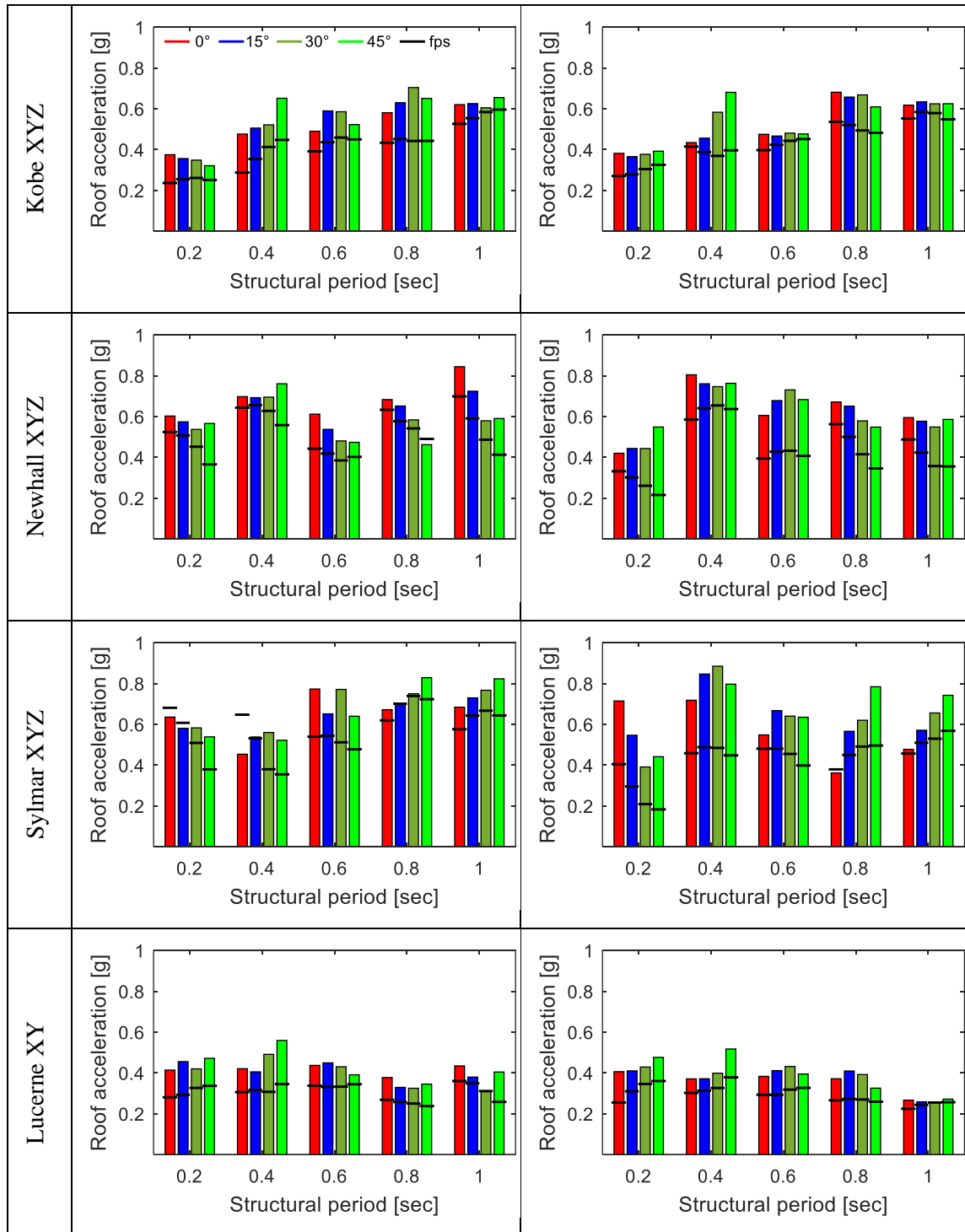


Figure 3.7. Maximum acceleration of the super-structure in X direction. Colored bars represent the XY-FPS, for $\beta = 0^\circ, 15^\circ, 30^\circ$ and 45° , black horizontal lines to the FPS devices, $T_b = 2.5$ s (on the left) and $T_b = 5.0$ s (on the right) .

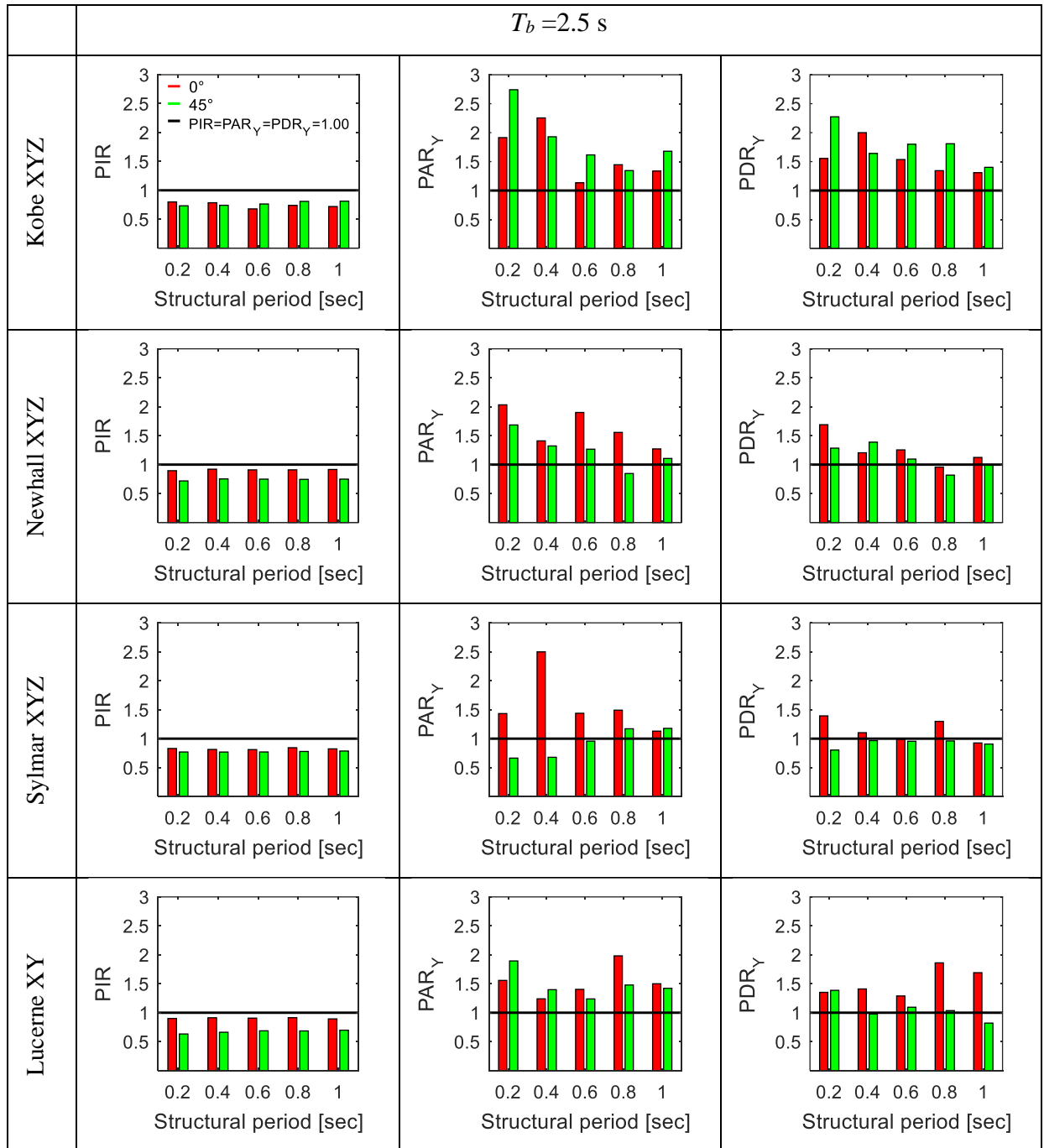


Figure 3.8. Response of PIR , PAR_y and PDR_y corresponding to Model A in Y direction.

Colored bars represent the XY-FPS for $\beta = 0^\circ$ and 45° , and black horizontal lines represent the $PIR = 1$, the $PAR_y = 1$ and the $PDR_y = 1$, respectively, for $T_b = 2.5$ seconds .

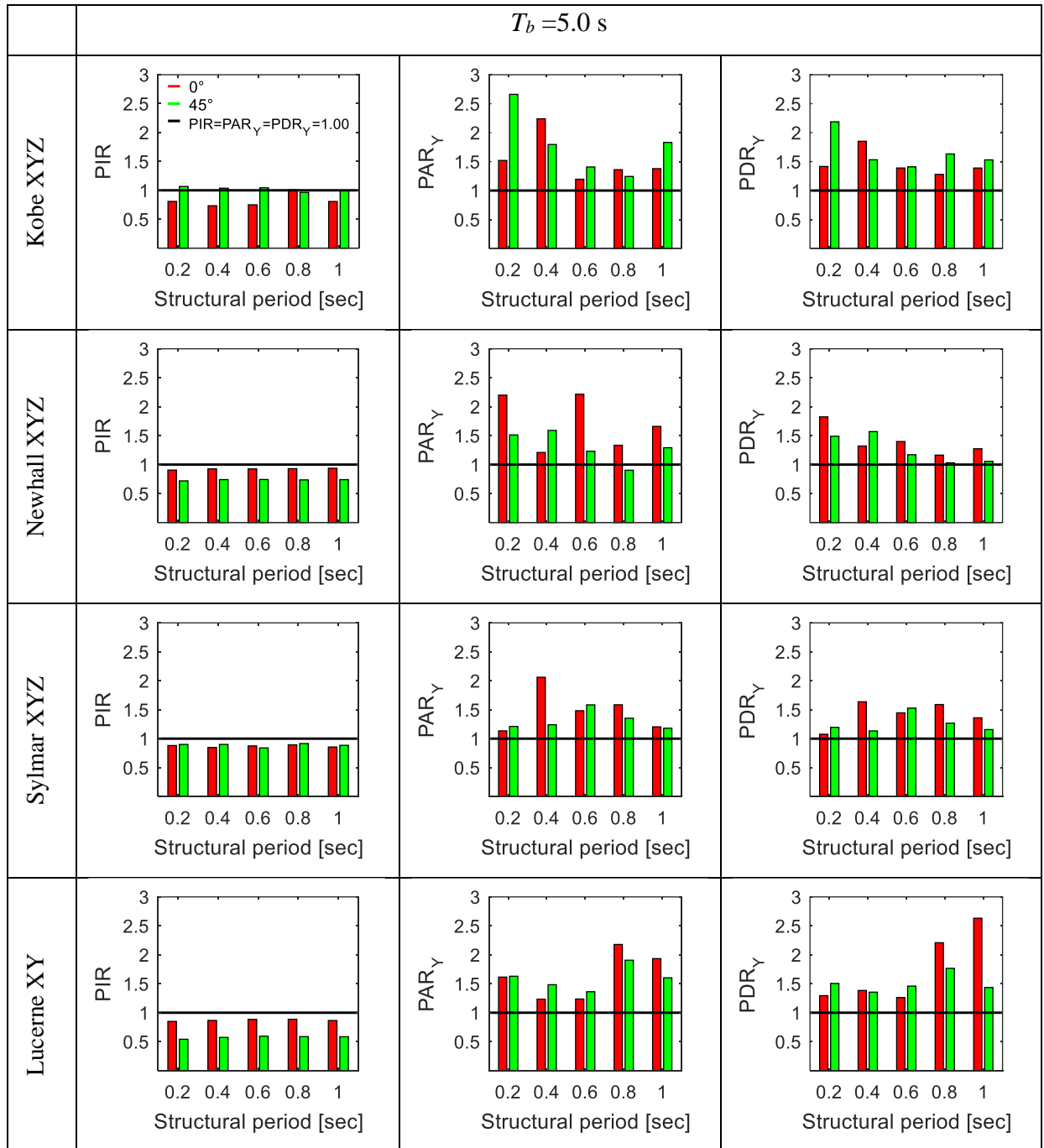


Figure 3.9. Response of PIR , PAR_y and PDR_y corresponding to Model A in Y direction.

Colored bars represent the XY-FPS for $\beta = 0^\circ$ and 45° , and black horizontal lines represent the $PIR = 1$, the $PAR_y = 1$ and the $PDR_y = 1$, respectively, for $T_b = 5.0$ seconds.

3.3.2 Results of Model B

The horizontal trajectory of the isolator #4 of a structure with $T_b = 2.5$ s, subjected to the Kobe earthquake record rotated at $\beta = 0^\circ$ and $\beta = 45^\circ$, is presented in Figure 3.10. As expected, the same behavior pattern of Model A is observed (see figure 3.4), i.e. the displacements of the XY-FPS isolators are lower due to the greater friction available, and more sensitive to the orientation of the earthquake, due to the anisotropy of frictional resistance.

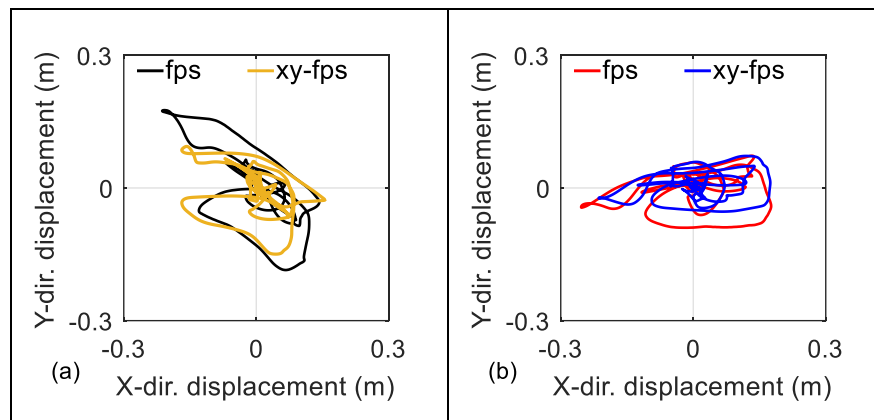


Figure 3.10. Horizontal trajectory of the isolator #4 for Model B ($T_b = 2.5$ s) subjected to the Kobe earthquake record rotated at: a) $\beta = 0^\circ$; and b) $\beta = 45^\circ$.

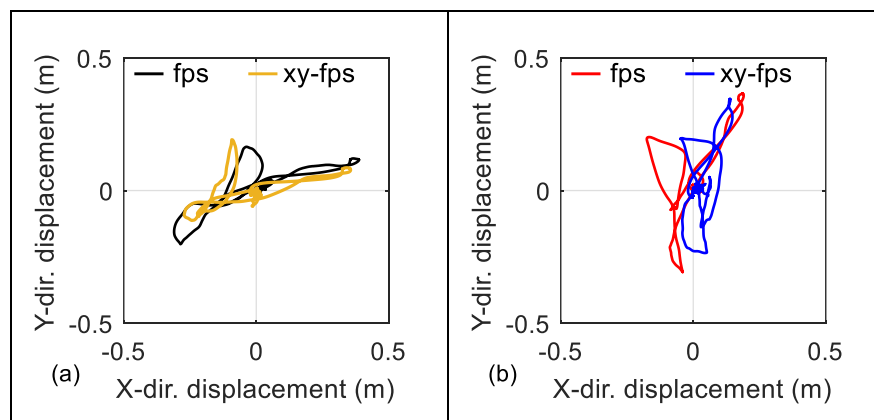


Figure 3.11. Horizontal trajectory of the isolator #4 for Model B ($T_b = 5.0$ s) subjected to the Sylmar earthquake record rotated at: a) $\beta = 0^\circ$; and b) $\beta = 45^\circ$.

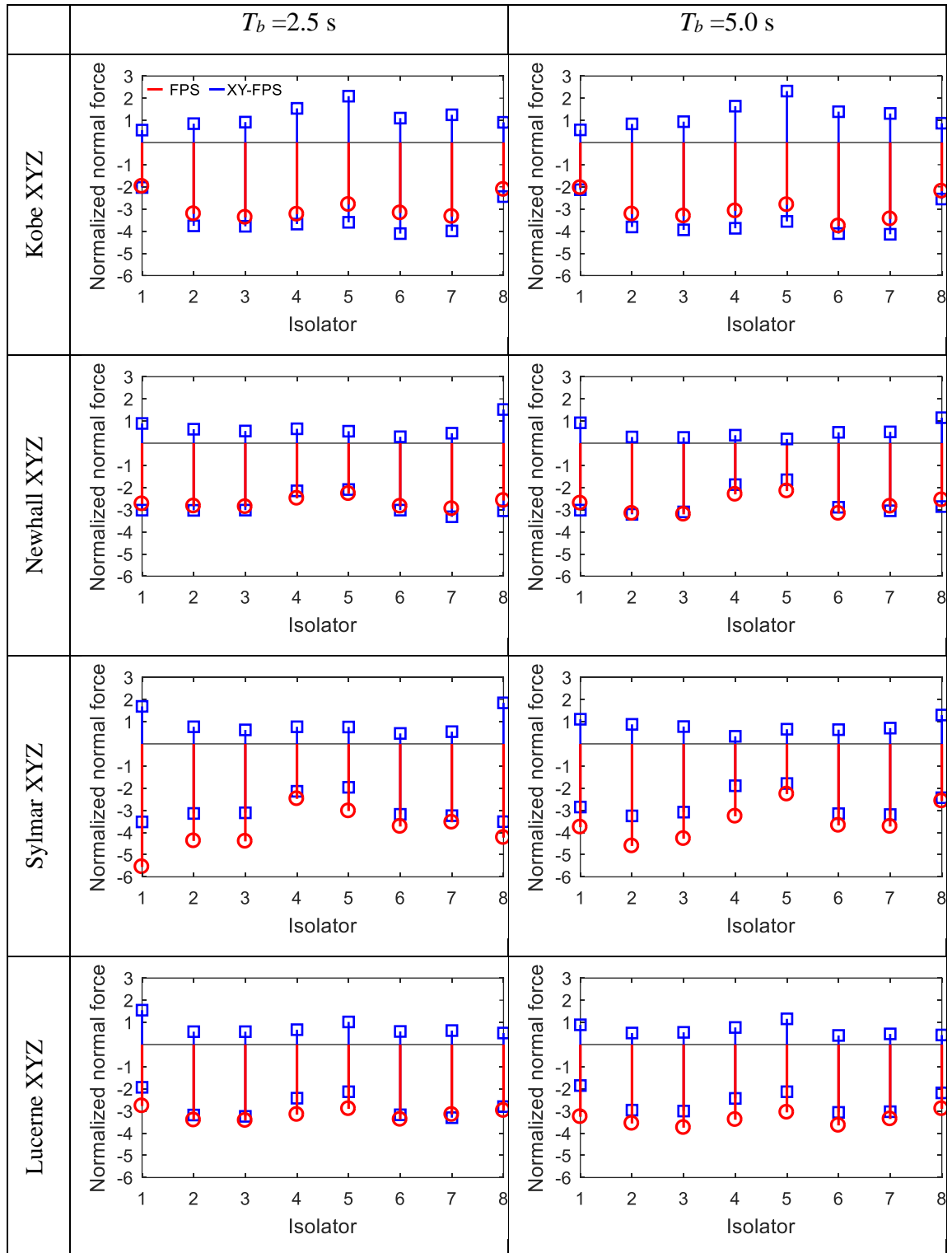
A similar result is presented in Figure 3.11, for the structure with $T_b = 5.0$ s, subjected to the Sylmar record.

One of the most important aspects to consider in this study is to quantify the uplift of the FPS devices. The maximum uplift values for the 8 isolators and for the 4 seismic records considered is shown in Table 3.6. Despite the great slenderness of the Model B and the impulsive nature of the records considered, the maximum uplift is less than 2 cm, with the exception of the structure with $T_b = 2.5$ s subjected to the Sylmar record, reaching a maximum uplift of 7.41 cm in the isolator #1. However, by increasing the period of isolation to $T_b = 5.0$ s, this uplift is reduced to 1.36 cm.

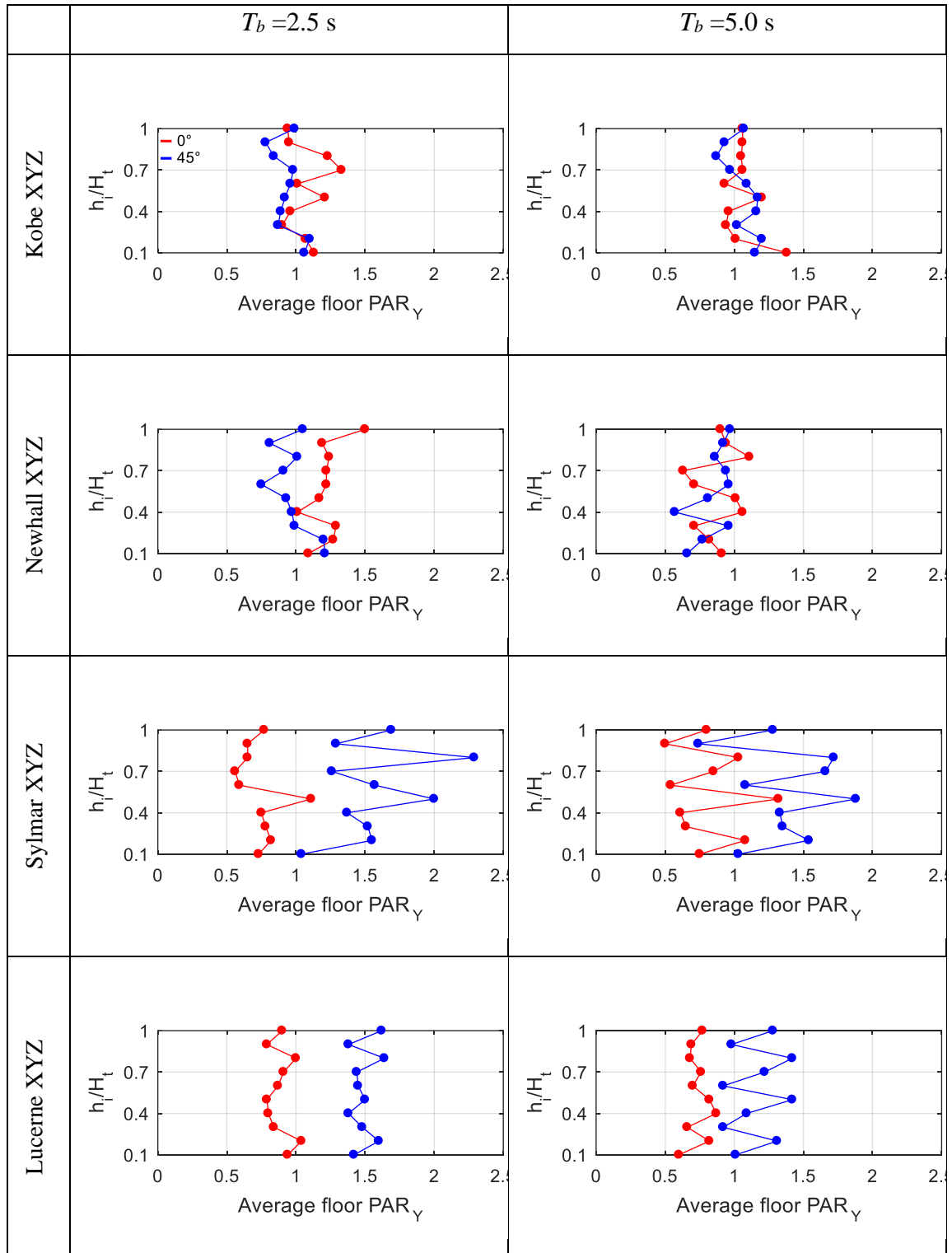
Table 3.6. Maximum uplift in cm ($\beta=0^\circ$)

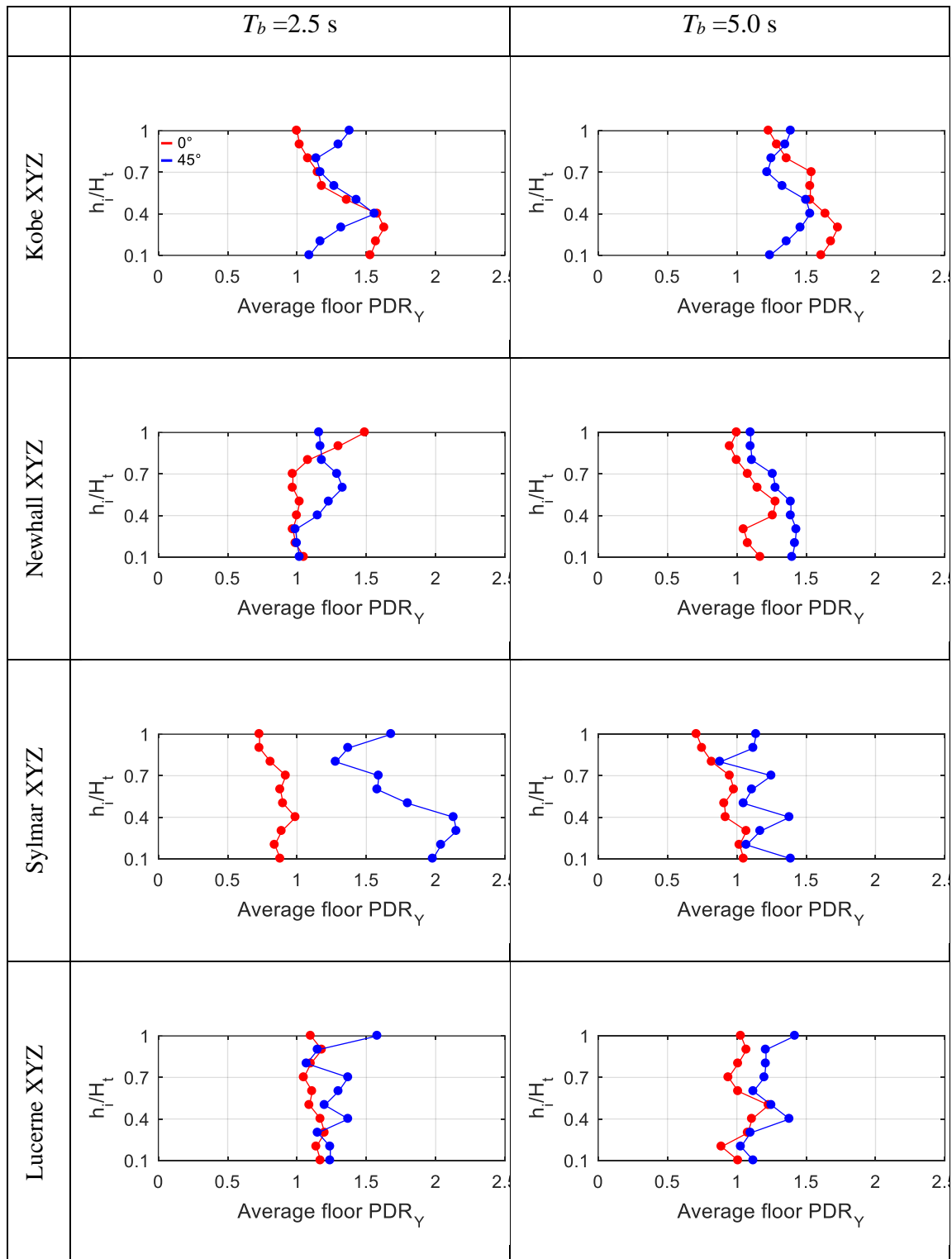
Isolator \ T_b (s)	Kobe		Lucerne		Newhall		Sylmar	
	2.50	5.00	2.50	5.00	2.50	5.00	2.50	5.00
1	0.15	0.33	1.53	1.44	0.99	0.62	7.41	1.29
2	0.20	0.23	0.28	0.31	0.70	0.17	6.76	1.02
3	0.47	0.34	0.23	0.23	0.58	0.09	6.43	0.66
4	1.02	0.70	0.66	0.63	1.10	0.33	6.24	0.58
5	1.51	1.01	1.50	1.71	0.74	0.24	3.26	0.47
6	0.89	0.50	0.28	0.37	0.11	0.09	3.60	0.61
7	0.51	0.62	0.32	0.29	0.23	0.12	3.81	0.90
8	0.55	0.74	0.47	0.37	0.97	0.54	5.26	1.36

Additionally, the maximum and minimum normalized axial load values for both types of isolators is shown in Figure 3.12. It can be seen that the maximum compression values are lower for the FPS devices (for example for the Kobe and Newhall records) when the uplift is relatively moderate as is depicted in Table 3.6. However, when the uplift is relatively large according to Table 3.6, the maximum compression values are greater for the FPS devices (for instance, for the Lucerne and Sylmar records), due to the effect of the impact after the uplift. Note also that the maximum tension values (positive values) in XY-FPS devices can be equal to or greater than the static load (initial condition). This implies a great demand for axial resistance for the internal mechanism that prevents uplifting, and therefore, the need to use tension-resistant foundation piles. The axial loads were normalized respect to the average static load (the total weight divided by eight).

Figure 3.12. Normalized normal forces corresponding to Model B ($\beta=0^\circ$).

Finally, Figure 3.13 and Figure 3.14 show the relationships between average floor peak acceleration ratio in Y direction and the average floor – peak inter-storey drift ratio in Y direction, corresponding to four seismic records considered for $\beta=0^\circ$ and 45° . As with Model A, an increase in the response of the superstructure with XY-FPS isolators is observed, which strongly depends on the angle of incidence of the earthquake. Figure 3.15 depicts the average floor peak acceleration in XY-FPS System, in Y-direction, for $\beta = 0^\circ$ and $\beta = 45^\circ$ and Figure 3.16 details the average floor peak effective drift in XY-FPS System, in Y-direction, for $\beta = 0^\circ$ and $\beta = 45^\circ$. The relation between the height of each floor and the total height of the structure is defined as h_i/H_t .

Figure 3.13. Average floor PAR_γ for $\beta = 0^\circ$ and 45° .

Figure 3.14. Average floor PDR_Y for $\beta = 0^\circ$ and 45° .

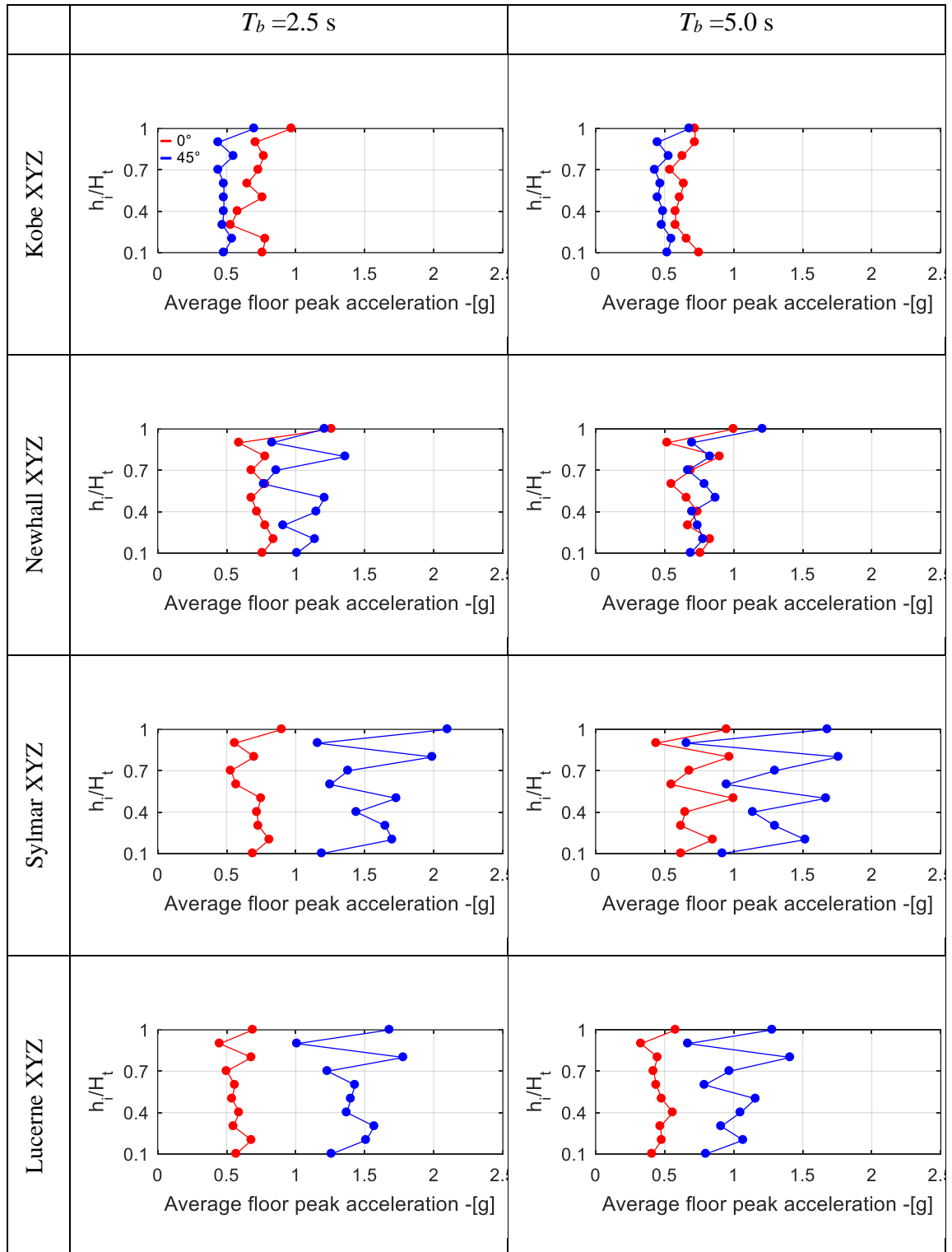


Figure 3.15. Average floor peak acceleration [g] in XY-FPS System, in Y-direction, for $\beta = 0^\circ$ and 45° .

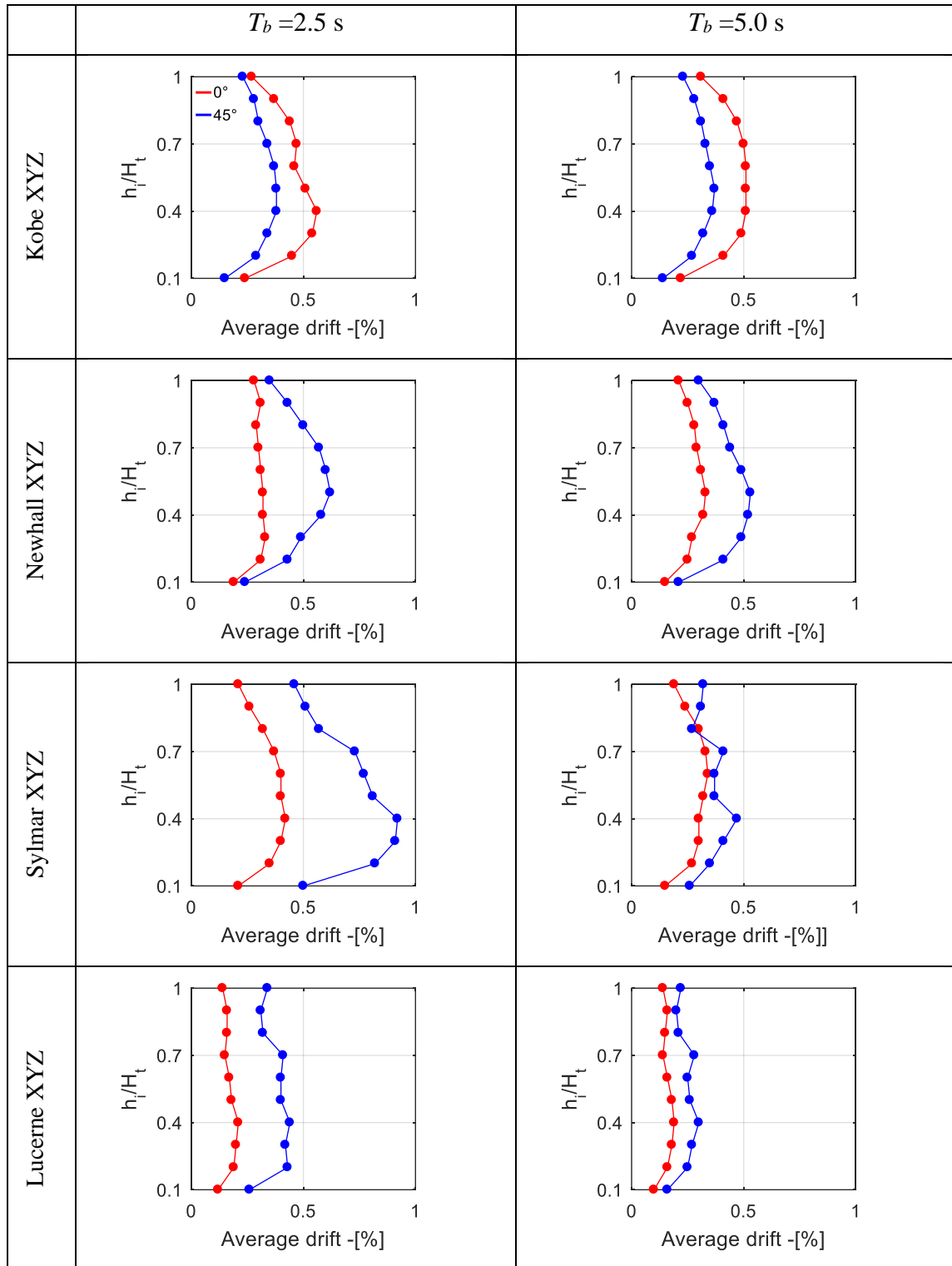


Figure 3.16. Average floor peak effective drift [%] in XY-FPS System, in Y-direction, for $\beta = 0^\circ$ and 45° .

3.3.3 Results of Model C

The results of Model C which considers the SSI condition (the model is detailed in section 3.1), using a different effective shear wave velocity of the soil and subjected to the selected ground motions, shall be analyzed and evaluated in this section. The values of the effective shear wave velocity of the soil are 200 *m/s*, 300 *m/s*, 400 *m/s* and 1000 *m/s*. To interpret the response of the Model C, the following relationships between the maximum time-history responses are defined:

$$P\hat{A}R(SSl)_x = \frac{a_{xo}^{(FPS-SSI)}}{a_{xo}^{(FPS-FIXED)}} \quad (3.3)$$

$$P\hat{A}R(SSl)_y = \frac{a_{yo}^{(FPS-SSI)}}{a_{yo}^{(FPS-FIXED)}} \quad (3.4)$$

$$P\hat{D}R(SSl)_x = \frac{d_{xo}^{(FPS-SSI)}}{d_{xo}^{(FPS-FIXED)}} \quad (3.5)$$

$$P\hat{D}R(SSl)_y = \frac{d_{yo}^{(FPS-SSI)}}{d_{yo}^{(FPS-FIXED)}} \quad (3.6)$$

where $P\hat{A}R(SSl)_j$ is the $-j$ direction average floor peak acceleration ratio considering the SSI ($j = X, Y$), being $a_{jo}^{(FPS-SSI)}$ and $a_{jo}^{(FPS-FIXED)}$ the $-j$ direction average floor peak absolute acceleration of each of floor with FPS including the SSI condition and FPS considering the fixed condition, respectively; and $P\hat{D}R_j$ is the $-j$ direction average floor peak drift ratio, being $d_{jo}^{(FPS-SSI)}$ and $d_{jo}^{(FPS-FIXED)}$ the $-j$ direction average floor peak inter-storey drift of each of floor with FPS considering the SSI condition and FPS including the fixed condition, respectively. The transverse axis is analyzed in this model.

It seems the consideration of the flexibility of the soil is a filter of higher frequencies, due to the axial forces of the isolator decreased when the effective shear wave velocity of the soil is lower. This behavior is depicted in Figure 3.17.

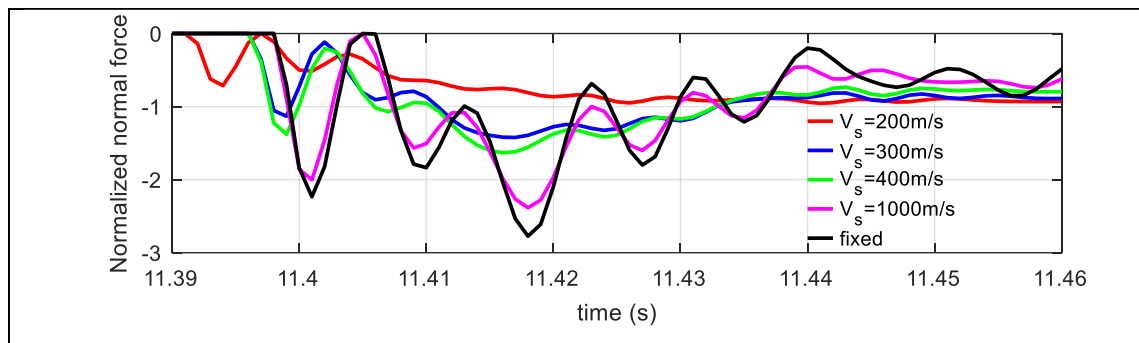


Figure 3.17. Normalized axial force at different shear- wave velocity in isolator # 1, for Model C with $T_b = 2.5$ s subjected to Lucerne record.

The $P\hat{A}R(SSI)_j$ and the $P\hat{D}R(SSI)_j$ were computed for all four selected ground motions. The variation of these ratios with effective shear wave velocity V_s is presented in Figure 3.18 and Figure 3.19. The average inter-storey drifts and accelerations ratios are minimally affected by the flexibility of the foundation when $V_s = 1000$ m/s in comparison to fixed model. The average responses are clearly sensitive to the flexibility of the soil in the range of $V_s = 200$ m/s to 400 m/s. In an overall sense, the average inter-storey drifts and accelerations ratios are minimized in cases of Sylmar and Lucerne and maximized for Kobe and Newhall when $V_s = 200$ m/s. It seems there is a relationship between the $P\hat{A}R(SSI)_y$ and $P\hat{D}R(SSI)_y$ and the values of the maximum uplift for each of the isolators. For instance, the greatest minimum values of $P\hat{A}R(SSI)_y$ and $P\hat{D}R(SSI)_y$ in Sylmar when $T_b = 2.5$ seconds is due to a maximum uplift of 7.41 cm (isolator 1). Therefore, the effects of vertical impacts activate the higher modes of the structure and the horizontal response increased in the rigid foundation (fixed model). As a result, the values of $P\hat{A}R(SSI)_y$ and $P\hat{D}R(SSI)_y$ are much less than one.

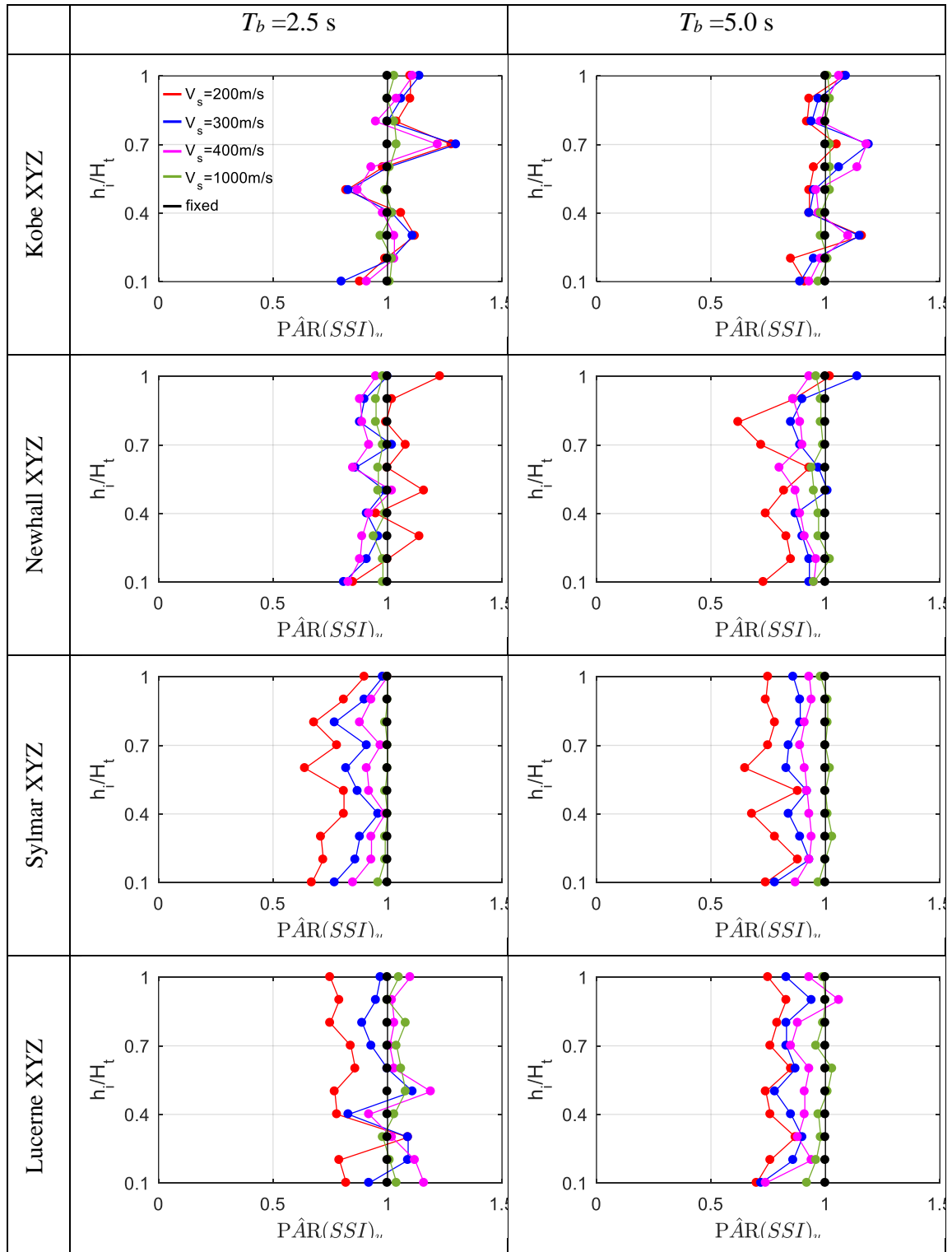


Figure 3.18. Average floor peak acceleration ratio of each of floor considering the SSI in Y-direction - $P\hat{A}R(SSl)_y$, for $\beta = 0^\circ$.

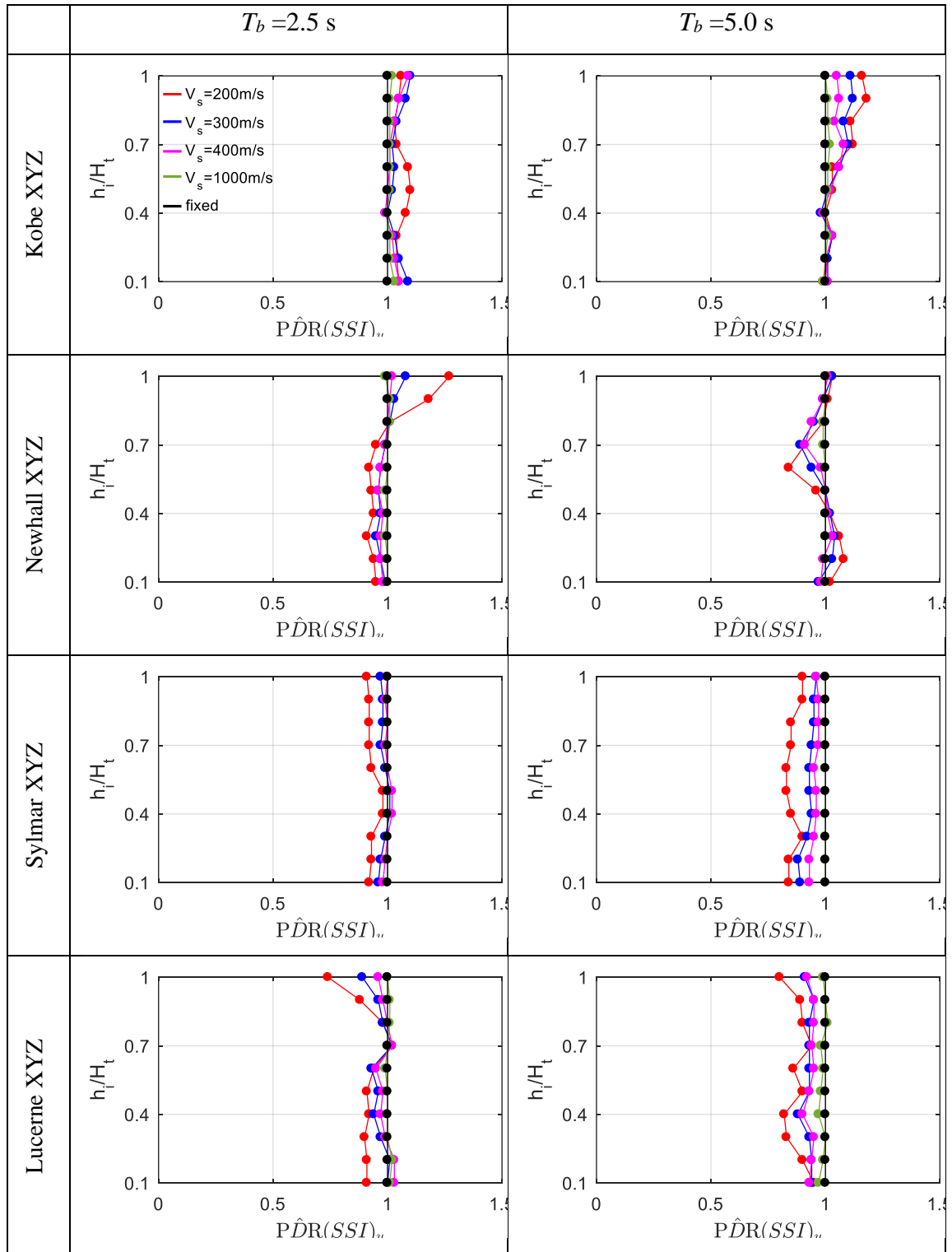


Figure 3.19. Average floor peak effective drift ratio of each of floor considering the SSI in Y-direction - $P\hat{D}R(SSi)_y$, for $\beta = 0^\circ$.

4. CONCLUSIONS

A complete mathematical formulation of the XY-FPS isolator has been considered. This formulation incorporates the most relevant aspects of the behavior of the device, such as frictional coupling and large deformations. It is shown that the pendulum effect (self-centering) of the XY-FPS isolator is practically identical to the FPS, that is, isotropic. In contrast, the frictional effect in the XY-FPS insulator is strongly anisotropic.

This study considered three models, The model A corresponds to a single-storey building isolated with one isolator (FPS and XY-FPS), the model B is a 10-storey, 3-bay-by-1-bay, plan symmetric reinforced concrete moment-frame structure, with eight isolators (FPS or XY-FPS) and the model C which is similar to Model B and consider only FPS isolators, including linear soil-structure interaction.

Minimum frictional resistance is obtained when the device is deformed in a direction parallel to any of the cylindrical sliding surfaces. Maximum frictional resistance occurs when the device deforms at a 45° to the orientation of the cylindrical sliding surfaces. The relationship between the maximum and minimum frictional resistance varies between 1.4 and 1.8, depending on the displacement.

As a consequence, the results obtained with models A and B indicate that the maximum displacements of the XY-FPS isolators are not only smaller, but they are also very sensitive to the directionality of the seismic motion, when compared with their counterparts with FPS.

In contrast, the superstructure accelerations are higher for the structures with XY-FPS. This should not be surprising, given that in general the lower the friction in the isolation system, the greater the response of the superstructure. However, there is an additional effect, which is the greater tendency of the XY-FPS to stick on one of the two cylindrical sliding surfaces, producing trajectories with sudden changes in direction. This happens because of the device tends to slide at the minimum frictional resistance directions, which are the parallel directions to the cylindrical surfaces (as shown in Figure 2.5). Instead, the FPS system tends to move in more rounded trajectories, due to the FPS has the same

frictional resistance in every direction (isotropic). Similar results may be appreciated in experimental studies.

Based on the results of Model B, it can be seen that the maximum compression normalized axial loads are lower for the FPS devices when the uplift is relatively moderate (less than 0.5 cm). On the other hand, when the uplift is relatively large (greater than 1.0 cm), the maximum compression normalized axial loads are greater for the FPS devices, due to the effect of the impact after the uplift. In contrast, the maximum tension normalized axial loads in XY-FPS devices can be equal to or greater than the static load. This implies a great demand for axial loads resistance for the internal mechanism that prevents uplifting, and the need to use tension-resistant foundation piles.

According to the results of model C, the overall response of slender structures with FPS isolators is not greatly affected by the flexibility of the foundation soil, as long as the maximum uplift is reasonable (say less than 20 mm). However, when excessively large uplifts occur, the subsequent impact activates higher modes of vibration, thus increasing floor accelerations. This effect is strongly attenuated as the foundation soil becomes more flexible (when V_s is less than 300 m/s), it is remarkable in the case of Sylmar and Lucerne records.

REFERENCES

- ATC and CUREE. 2012. Soil -structure interaction for building structures. Report No. NIST GCR 12-917-21, CA, USA.
- Al-Huassaini, T.M., Zayas, V.A, & Constantinou, M.C. (1994). *Seismic isolation of multi-story frame structures using spherical sliding isolation systems* (Tech. Rep). State University of New York at Buffalo, CA: National Center for Earthquake Engineering Research.
- Almazán, J. L. (2001) Torsión accidental y natural de estructuras aisladas con el sistema de péndulo de fricción. (Doctoral dissertation, in Spanish), Pontificia Universidad Católica de Chile.
- Almazán, J.L., & De la Llera, J.C. (2003) Physical model for dynamic analysis of structures with FPS isolators, 32(8): 1157-1184. *Earthquake Engineering and Structural Dynamics*.
- Arima, F.I., Suzuki, T., Takase, N., & Harada, H. (2000). *A development of a new technology for base-isolated buildings using cross linear bearings*. Auckland, New Zealand, 12th World Conference on Earthquake Engineering.
- Auad, G., & Almazán, J.L. (2021). Lateral impact resilient double concave friction pendulum (LIR-DCFP) bearing: Formulation, parametric study of the slider and three-dimensional numerical example. *Engineering Structures*, 233(2021) 111892.
- Bedriñana, L.A., Tani, M., & Nishiyama, M. (2021). Deformation and cyclic buckling capacity of external replaceable hysteretic dampers for unbonded post-tensioned precast concrete walls. *Engineering Structures*, 235(2021) 112045.
- Constantinou, M.C., Mokha, A., & Reinhorn, A.M. (1990). Teflon bearings in base isolation. II: Modeling. *Journal of Structural Engineering, ASCE* 116(2), 455-474.
- Constantinou, M.C., Whittaker, A.S., Kalpakidis, Y., Fenz, D.M., & Wam, G.P. (2007). *Performance of Seismic Isolation Hardware under Service and Seismic Loading* (Tech. Rep). State University of New York at Buffalo, CA: Multidisciplinary Center for Earthquake Engineering Research.
- Constantinou, M.C., & Capen, S.P. (2019). *Testing of seismic protective system hardware: significance, scaling and similarity*. Athens, Greece, 4th National Conference on Earthquake Engineering and Engineering Seismology.

Dao, N.D. (2012). *Seismic response of a full-scale 5-story steel frame building isolated by triple pendulum bearings under 3D excitations* (Doctoral dissertation). University of Nevada, Reno.

Dao, N.D., & Ryan, K.L. (2020) Soil-structure Interaction and Vertical-horizontal Coupling Effects in Buildings Isolated by Friction Bearings. *Journal of Earthquake Engineering*. DOI: 10.1080/13632469.2020.1754969.

Giammona, A. P., Ryan, K. L., & Dao, N. D. (2015). Evaluation of Assumptions Used in Engineering Practice to Model Buildings Isolated with Triple Pendulum Isolators in SAP2000. *Earthquake Spectra*, 31(2), 637–660.

Griffith, M.C., Kelly, J.M., Coveney, V.A., & Koh C.G (1988). *Experimental evaluation of seismic isolation of medium rise structures subject to uplift*. (Tech. Rep). University of California, Berkeley, CA: Earthquake Engineering Research Center.

Griffith, M.C., Aiken, J.D., & Kelly J.M (1988). *Experimental evaluation of seismic isolation of a 9-story braced steel frame subject to uplift*. (Tech. Rep). University of California, Berkeley, CA: Earthquake Engineering Research Center.

Hazaveh, N.K., Chase, J.G., Rodgers, G.W., Pampanin, S., & Kordani, R. (2018). Seismic Behaviour of a Self-Centering System with 2 -4 viscous damper. *Journal of Earthquake Engineering*. DOI: 10.1080/13632469.2018.1453415.

Huang, S., Skokan, M., Islam, S. (2006). Essential facility benefits from new base isolation technology. Structures Congress 2006, St. Louis, Missouri, United States, *ASCE*.

Huffmann, G.K. (1984). Full base isolation for earthquake protection by helical springs and viscodampers. *Nuclear Engineering and Design*, 84(3), 331-338.

Kasalanati, A., & Constantinou, M.C. (1999). *Experimental study of bridge elastomeric and other isolation and energy dissipation systems with emphasis on uplift prevention and high velocity near-source seismic excitation* (Tech. Rep). State University of New York at Buffalo, CA: Multidisciplinary Center for Earthquake Engineering Research.

Logiadis, I.S.E. (1996). *Application of vertical unbonded tensioned prestressed tendons in the seismic isolation of structures* (Doctoral dissertation). Technische Universitat Munchen.

Marin, C.C. (2006). *Experimental and analytical study of the xy-friction pendulum (xy-fp) bearing for bridge applications* (Doctoral dissertation). State University of New York at Buffalo.

Mosqueda, G., Whittaker, A.S., & Fenves, G.L. (2004). Characterization and modeling of friction pendulum bearing subjected to multiple components excitations. *Journal of Structural Engineering, ASCE*, 130(3), 433-442.

Nawrotzki, P., Kostarev, V., Siepe, D., & Morozov, D. (2019), 3-D base control systems for the seismic protection of structures, St. Petersburg, Russian Federation, 16th Conference on Seismic Isolation, Energy Dissipation and Active Vibration Control of Structures, Anti-Seismic Systems International Society: ASSISi.

Nielsen, G., Rees, S., Dong, B., Chok, K., Fatemi, E., & Zekioglu, A. (2017). *Practical implementation of ASCE-41 and NLRHA procedures for the design of the LLUMC replacement hospital*. SEAOC Convention Proceedings.

Novak, M., & Henderson, P. (1989). Base isolated buildings with soil-structure interaction. *Earthquake Engineering and Structural Dynamics* 18(6), 751-765.

Pais, A., & Kausel, E. (1988). Approximate formulas for dynamic stiffnesses of rigid foundations, 7(4), 213-227. *Soil Dynamics and Earthquake Engineering*.

Restrepo, J.I., Mander, J., & Holden, T.J. (2001). *New generation of structural systems for earthquake resistance*. Wellington, New Zealand, Annual Technical Conference, New Zealand Society for Earthquake Engineering.

Reyes, S.I., & Almazán, J.L. (2020). A novel device for a vertical rocking isolation system with uplift allowed for industrial equipment and structures. *Engineering Structures*, 214(2020), 110595.

Roussis, P.C. (2004). *Experimental and analytical studies of structures seismically isolated with an uplift-restraint isolation system* (Doctoral dissertation). State University of New York at Buffalo.

Roussis, P.C., & Constantinou, M.C. (2006). Uplift-restraint friction pendulum seismic isolation system. *Earthquake Engineering and Structural Dynamics*, 29(7), 125-126.

Roussis, P.C., & Constantinou, M.C. (2006). Experimental and analytical studies of structures seismically isolated with an uplift-restraint friction pendulum system. *Earthquake Engineering and Structural Dynamics* 29(7), 125-126.

Ryan, K.L., Coria, C.B., & Dao, N.D. (2012). *Large scale earthquake simulation of hybrid lead rubber isolation systems designed with consideration of nuclear seismicity*. (Tech. Rep). United States Nuclear Regulatory Commission.

Ryan, K.L., Soroushian, S., Maragakis, E.M., Sato, E., Sasaki, T., & Okazaki, T. (2016). Seismic simulation of an integrated ceiling-partition wall-piping system at E-Defense. I:

Three-dimensional structural response and base isolation. *Journal of Structural Engineering, ASCE* 142(2), 04015130.

SAP2000. © 2021. Computers & Structures, Inc. Structural and Earthquake Engineering Software.

Staton, J., Stone, W., & Cheok, G.S. (1997). A hybrid precast frame for seismic regions. *PCI Journal*, 42 (2), 20-32.

Tsopelas, P.C., Constantinou, M.C., & Reinhorn, A.M. (1994). *3D-BASIS-ME: Computer program for nonlinear dynamic analysis of seismically isolated single and multiple structures and liquid storage tanks*. (Tech. Rep). State University of New York at Buffalo, CA: Multidisciplinary Center for Earthquake Engineering Research.

Tsopelas, P., & Constantinou, M.C. (1994). *NCEER-TAISEI Corporation research program on sliding seismic isolation systems for bridges: experimental and analytical study of systems consisting of sliding bearings and fluid restoring force/damping devices* (Tech. Rep). State University of New York at Buffalo, CA: National Center for Earthquake Engineering Research.

Wichman, S. (2018). *Large-Scale Dynamic Testing of Rocking Cross Laminated Timber Walls* (Master dissertation). University of Washington, Seattle, WA.

Zayas, V., & Low, S. (2006). Patent number 8484911 B2, July 16, 2013, publication number US 2006/0174555 A1.

Zayas, V. (2014). Earthquake Protection Systems (EPS) Qualifications.